NASA/TP-20205011762

Charging Experiments and Filtration Testing on Facemask Materials

Towards Goals of Full Performance Restoration of Used N95 Masks and Enhancement of Common-Fabric Facemasks

Brian D. Bertram, Juan H. Agui, and Richard A. Kelsch
Glenn Research Center, Cleveland, Ohio

Douglas O. Doza
HX5, LLC, Brook Park, Ohio

Gordon M. Berger
Universities Space Research Association, Cleveland, Ohio

Robert D. Green
Glenn Research Center, Cleveland, Ohio

April 2022

NASA STI Program . . . in Profile

Since its founding, NASA has been dedicated to the advancement of aeronautics and space science. The NASA Scientific and Technical Information (STI) Program plays a key part in helping NASA maintain this important role.

The NASA STI Program operates under the auspices of the Agency Chief Information Officer. It collects, organizes, provides for archiving, and disseminates NASA's STI. The NASA STI Program provides access to the NASA Technical Report Server—Registered (NTRS Reg) and NASA Technical Report Server—Public (NTRS) thus providing one of the largest collections of aeronautical and space science STI in the world. Results are published in both non-NASA channels and by NASA in the NASA STI Report Series, which includes the following report types:

- TECHNICAL PUBLICATION. Reports of completed research or a major significant phase of research that present the results of NASA programs and include extensive data or theoretical analysis. Includes compilations of significant scientific and technical data and information deemed to be of continuing reference value. NASA counter-part of peer-reviewed formal professional papers, but has less stringent limitations on manuscript length and extent of graphic presentations.

- TECHNICAL MEMORANDUM. Scientific and technical findings that are preliminary or of specialized interest, e.g., "quick-release" reports, working papers, and bibliographies that contain minimal annotation. Does not contain extensive analysis.

- CONTRACTOR REPORT. Scientific and technical findings by NASA-sponsored contractors and grantees.

- CONFERENCE PUBLICATION. Collected papers from scientific and technical conferences, symposia, seminars, or other meetings sponsored or co-sponsored by NASA.

- SPECIAL PUBLICATION. Scientific, technical, or historical information from NASA programs, projects, and missions, often concerned with subjects having substantial public interest.

- TECHNICAL TRANSLATION. English-language translations of foreign scientific and technical material pertinent to NASA's mission.

For more information about the NASA STI program, see the following:

- Access the NASA STI program home page at http://www.sti.nasa.gov

- E-mail your question to help@sti.nasa.gov

- Fax your question to the NASA STI Information Desk at 757-864-6500

- Telephone the NASA STI Information Desk at 757-864-9658

- Write to:
  NASA STI Program
  Mail Stop 148
  NASA Langley Research Center
  Hampton, VA 23681-2199

NASA/TP-20205011762

Charging Experiments and Filtration Testing on Facemask Materials

Towards Goals of Full Performance Restoration of Used N95 Masks and Enhancement of Common-Fabric Facemasks

Brian D. Bertram, Juan H. Agui, and Richard A. Kelsch
Glenn Research Center, Cleveland, Ohio

Douglas O. Doza
HX5, LLC, Brook Park, Ohio

Gordon M. Berger
Universities Space Research Association, Cleveland, Ohio

Robert D. Green
Glenn Research Center, Cleveland, Ohio

National Aeronautics and
Space Administration

Glenn Research Center
Cleveland, Ohio 44135

April 2022

Acknowledgments

Useful technical discussions occurred with Warren Jasper, Ron Schaffer, and Bruce Banks. Some of the equipment used in the charging attempts was provided by Pete Bonacuse and Timothy Peshek. General support of the project was provided by Marla Pérez-Davis, Laurence Sivic, Timothy McCartney, and Steve Sinacore.

Level of Review: This material has been technically reviewed by technical management.

Available from

NASA STI Program
Mail Stop 148
NASA Langley Research Center
Hampton, VA 23681-2199

National Technical Information Service
5285 Port Royal Road
Springfield, VA 22161
703-605-6000

This report is available in electronic form at http://www.sti.nasa.gov/ and http://ntrs.nasa.gov/

Contents

Charging Experiments and Filtration Testing on Facemask Materials

Towards Goals of Full Performance Restoration of Used N95 Masks and Enhancement of Common-Fabric Facemasks

Brian D. Bertram, Juan H. Agui, and Richard A. Kelsch
National Aeronautics and Space Administration
Glenn Research Center
Cleveland, Ohio 44135

Douglas O. Doza
HX5, LLC
Brook Park, Ohio 44142

Gordon M. Berger
Universities Space Research Association
Cleveland, Ohio 44135

Robert D. Green
National Aeronautics and Space Administration
Glenn Research Center
Cleveland, Ohio 44135

Summary

Different techniques have been developed for sanitizing N95 masks while retaining whatever charge remains on them. However, these sanitizing methods do not address the fact that the electrical charge, filtration efficacy, and breathability of such masks may be expected to degrade during long-term use based on mechanisms known in the literature. In this study, approaches to electrically (re)charge facemask filter materials were explored in response to the COVID–19-induced shortage of N95 masks. The effort consisted of charging experiments followed by filtration testing conducted at the coupon level during a month-long period (May 2020) and subsequently a literature review. The main focus of the experiments was to develop a recharging technique that could eventually be adapted and used as part of a broader full-performance restoration process for used N95 masks. This process might employ a simple wash by soapy water or alcohol as a preceding step for sanitization and declogging. Most tested coupons were, therefore, nonwoven meltblown fibrous polypropylene (PP) filter media extracted from decades old N95 masks. Keeping in mind commonly used cloth facemasks, limited trials were also performed with some commercially available fabrics. Charging was done at elevated temperature and was followed by cooling to freeze in the applied charges produced from either corona discharges using different electrode configurations and parameter combinations or from triboelectric rubbing. Charging was also focused on using potentially scalable equipment, for example, Van de Graaff generators or consumer ionic hair products. Some degree of success was achieved with one of the fabrics and the PP filter media, which was first purposefully discharged to have typical filtration efficiency (FE) of ~35 percent. Numerous attempts at corona charging discharged media resulted in FE ≥ 80 to 85 percent. Some measure of charge robustness was also established via stable performance during loading testing. However, results where FE ≥ 90 percent were not reliably repeatable, and no results met the FE ≥ 95 percent goal due to shortcomings of the charging process. The best three trials for PP media met the FE ≥ 90 percent criteria within statistical variation, amounted to a small percentage of the trials relying on an ionic hair dryer, and are attributed to good embedding of charges via aerodynamic force. Triboelectric charging with a hair straightener significantly enhanced the viability of one of the polyester fabrics where measured FE increased from 19 up to 46 percent while maintaining a reasonably low pressure drop.

1.0 Introduction

During the COVID–19 global pandemic, there have been concerns about shortages of personal protective equipment used by healthcare providers including N95 masks. These masks are extremely useful for reducing the risk of transmission of the respiratory virus when close contact occurs between the uninfected and COVID–19 positive individuals. As a result, much work has been done to develop best practices for decontamination and reuse of used N95 masks that are already

on hand. This report describes one such project at NASA Glenn Research Center where the goal was to develop a charging technique for mask filter media that could eventually be transitioned and applied to full masks.

As will be described in detail, the performance of N95 masks may be adversely impacted by reuse, some decontamination methods, and improper storage. This section provides an elementary background in the science underlying the performance and fabrication of the special electrically charged filter material within N95s, as well as relevant mechanisms by which the utility of N95 masks for users and the public may plausibly be degraded. Current decontamination techniques do not address many of these mechanisms, but a viable recharging process could be paired with a simpler decontamination method that does (due to being unconstrained by the need to preserve charge). As such, a two-step process for complete performance restoration of N95s is envisioned. This backdrop will allow for a full understanding and appreciation of the experimental work and the main goal of a viable and scalable recharging process for N95s, as well as the side effort for electrically charging commercially available fabrics.

1.1 Performance of N95s and Mechanisms Thereof

Proper background begins with the impressive performance of the engineered filter material employed in N95s. This is often described with two metrics, filtration efficiency (FE) and pressure drop. The "95" part of the N95 designation signifies that a new mask exhibits at least 95 percent FE. This means that it captures at least 95 percent of particles when tested per standard National Institute for Occupational Safety and Health (NIOSH) procedure (Ref. 1) simulating a perfectly fitted mask in an otherwise worst-case scenario of the most penetrating particle size, ~0.050 μm (Ref. 2). For other particle sizes, N95 filtration efficiency exceeds 95 percent. Commonly, FE of new masks (Refs. 2 and 3) is approximately 99 percent, that is, penetration is only about 1 percent. This may help ensure that masks continue to meet the 95 percent requirement even if they sit idle for a few years before their first use. New N95s also have a very low pressure drop, and thus present low resistance to breathing because their filter layers have porosity of ~90 percent (Refs. 4 and 5).

In the context of a respiratory-virus pandemic, one should also consider the performance of the N95s in circulation in terms of their overall impact on public health and the associated protection against virus transmission that they afford. In this broader view, we recognize that the outstanding initial performance provided for by the engineered filter material of N95s may be (1) eroded during long-term use by various plausible mechanisms, (2) partially circumvented by mask-face seal leakage, or (3) fully undermined by owners choosing not to wear their masks. In Section 1.4, these issues are further examined.

N95 masks have four main mechanisms of capturing particles onto the fibers that comprise their filter layer. These are direct interception, inertial impaction, convective Brownian diffusion, and electrostatic attraction (Ref. 6). The first three mechanisms are essentially mechanical in nature, whereas the latter is not. It refers to particles in the air being electrostatically attracted to the electrically charged fibers of the filter layer (Ref. 6). This report pertains primarily to the electrostatic mechanism, which is typically absent in common-fabric facemasks, although it has been considered (Ref. 7). It is this mechanism that allows for the highly efficient capture of fine particles while simultaneously maintaining a low pressure drop (i.e., easy breathability) through the mask.

The electrically charged characteristic of fibers in N95 mask filters is the most important contributor to their outstanding performance. In one study that tested electrostatic filters of polypropylene (PP) fibers (the material used in N95 masks), electrostatic filtration was calculated to be responsible for 61 to 92 percent of performance, whereas mechanical filtration provided the remainder (Ref. 8). The electrostatic contribution is particularly important in the 0.15- to 0.5-μm size range where collection by other mechanisms is relatively difficult (Ref. 9). It is also important to note that the electrostatic mechanism operates on both charged and electrically neutral particles in the air. Many of the particles in air are electrically charged; the fraction of charged particles reflects the radius-dependent probability of a given particle having one or more extra or missing electrons. This is well-described by a modified version (Ref. 10) of the Fuch's model (Ref. 11) for the steady-state distribution of charge. For example, for a particle size of 1 μm (which is much smaller than the pores of cloth masks), roughly ~85 percent of particles are charged. A filter may also electrostatically capture neutral particles by induction (Ref. 6). In this process, neutral particles are polarized by and then attracted to the electric field surrounding charged fibers. This phenomenon is reminiscent of the attraction of unmagnetized iron filings to a magnet and actually depends on the gradient of the electric field not the field itself (Ref. 12). Perhaps the most convincing argument for the electrostatic mechanism's importance is made by empirical comparison to its absence. In one study, aerosol penetration was measured at 0.01 and 50 percent for charged and uncharged filters of similar structure, respectively (Ref. 6). In another study, similarly dramatic differences were demonstrated as a function of particle size (Ref. 13). In yet another study, a filter comprising PP fibers and specialty fibers experienced a reduction in FE from 97.8 to 20 percent after removing the electrical charge from the fibers (Ref. 14). A similar result was demonstrated with a filter made only of PP fibers; penetration increased from <5 to ~75 percent (Ref. 8).

The electrostatic mechanism is active for as-received N95 masks because the PP fiber filter material within the masks exists in an electret state as a result of the manufacturing process. An electret is a dielectric material (an electrical insulator) that has a semipermanent external electrical dipole moment. Electrets can be classified as being dipolar or being due to real charge. In dipolar electrets, there is a semipermanent preferred (nonrandom) orientation of microscopic electrical dipole moments associated with microscopic charge separations in or on the material; the material itself has no excess charges and is overall charge-neutral. In real-charge electrets, excess charges (that are not native to the material) exist due to injection or embedding (Ref. 12). This results in a finite net charge on the material that is either positive or negative except in the (unlikely) case where the numbers of excess charges of opposite signs counterbalance exactly. Although there are many different N95 masks by many different manufacturers, and the particulars of each may involve proprietary information, N95 masks are generally understood to utilize real-charge electrets (Ref. 15).

1.2 Charging Processes

Electrets can be created by "freezing in" an applied charge or a dipolar configuration having preferred orientation. This is often done by applying charge, for example, via a strong electric field, to a warmed (Ref. 16) or melted (Ref. 17) electrically insulating material and maintaining the field during cooling until the temperature is sufficiently below the temperature during charging. The frozen-in charges are commonly described as "trapped" because they may dissipate very slowly at low temperatures, such as room temperature. As discussed more later, detrapping or neutralization of the trapped charge can occur by various means and generally occurs faster at higher temperatures.

There are different ways of producing electrets. While a lot of early work (Refs. 16 to 19) focused on charging waxes using dielectric absorption in simple capacitor setups, methods for charging filter materials such as those for N95s have become more advanced. For example, processes for polymer fiber electret filters include triboelectric charging, corona discharge, and electrostatic fiber spinning, or electrospinning (Ref. 14). Tribocharging occurs via friction and has been demonstrated via the use of dissimilar fibers during textile carding and alternatively by the evaporation or suction of water out of fabric in a patented process (Ref. 14). Corona charging may be performed on the fibers themselves or on fabrics (Refs. 14, 20, and 21). Such fabrics may be nonwovens comprising meltblown or spun-bond fibers (Ref. 14). In electrospinning, the charging of the polymer and spinning to form fiber occurs in a single step. Fabric formation then immediately follows as the newly electrospun fibers are collected onto a flat surface where they form a nonwoven web (Ref. 14).

Different electrode configurations may be used for the corona charging of fibers already amassed into nonwoven fabrics (Ref. 21). In one approach, a high-voltage power supply energizes a sharp pin or row of such pins. Generally, the voltage should be much higher than that needed to ionize the pin surface(s) but lower than the arcing voltage (Ref. 21). The enhancement of the electric field caused by the high curvature of the pin tips increases the local ionization of the air, and electron production therein. For a negative polarity corona, the electron avalanche is driven by the photoelectric effect at the surface of the active electrode. Reaction of these electrons with gas molecules in the air produces negative air ions. Embedding of charges into the target electret material is achieved by aerodynamic force from an assisting airstream, the electrostatic force from the applied electric field, or some combination of the two (Ref. 21). Estimates of the electric field distribution can be made for different geometries but this distribution is also complicated by other factors such as air content, pressure, temperature, and discharge concentration. In some cases, a triode configuration using a metal screen near the media is employed to help control the electric potential of the media (Refs. 22 and 23).

High charging efficiency usually requires experimentation for optimization of parameters to achieve an appropriate electric field distribution and discharge current (Ref. 21). One may imagine that these may include current, voltage, tip radius, pin-tip metal durability and electronic work function, residence time, the ground electrode geometry, air pressure, velocity, and for hot charging, temperature and cooling rate. Charging may be performed while the material is hot or cold. As has been noted (Ref. 24), most hot and cold charging methods fail to develop the necessary charge density for very high levels of FE. Charging bleeding off the material with time is an additional problem for most cold charging processes (Ref. 24). Low humidity has been proposed to increase the retention of charge (Ref. 22). Negative rather than positive coronas have been found to be preferred for charging nonwoven PP media and this has been attributed to favorability of the ionic species involved (Ref. 22). Bipolar charging, in which media is imparted with charges of both polarities, has also been patented (Ref. 24). The disclosure did not explain the mechanisms for the observed improvements to charge density and lifetime, and here it is proposed that excess charges of opposite polarity may energetically stabilize each other if the electrical conductivity of the host material is low enough to inhibit recombination of opposite-sign point charges. Also, it is suggested here that filtration performance of bipolar electret filters may be enhanced by microscopic gradients of electric field associated with distributions of opposite-sign point charges that are intermingled and closely interfacing.

1.3 Microscopic Charged States and Effects of Time and Humidity in Storage

To facilitate charging processes, it would be helpful to know just how exactly the material becomes charged and where the charges reside in the electret material. Yet, despite the practical knowledge described previously, the industrial use of electrets beginning 40 years ago, and the widespread proliferation of N95 masks, there is little knowledge of the microscopic mechanisms for charge storage and the precise nature of the trap states in polymer electret materials in the public domain (Ref. 25). For corona-charged PP fibers, the exact locations and exact distribution of the trapped charges remains generally unknown (Ref. 12). Precise mapping is difficult because measurements of electric field at the nanometer scale is nontrivial (Ref. 12) and the distribution of stored charges tends to be very dilute (Ref. 25). Literature often refers to charges existing on the surface (Refs. 12, 22, and 26) of or on the periphery (Ref. 27) of such fibers rather than within the bulk. Indeed, any charge stored in the bulk of fibers would logically exert less external influence due to dielectric screening from the encompassing fiber material. However, charge storage has been determined to occur within the bulk of non-PP polymers, that is, fluoropolymers (Refs. 25 and 28 to 30), including cases where charge was imparted via corona discharge (Refs. 29 and 30), and where the bulk volume charge was determined to be uniformly distributed (Ref. 28).

Although a precise general understanding of charge storage mechanisms has remained elusive, some candidate microscopic features for trap sites have emerged. These include amorphous-crystalline boundaries, defects, and impurities (Refs. 27 and 31). Polymerization catalysts, additives, and radicals may also be relevant (Ref. 25). In one study, the degree of crystallization in corona-charged PP correlated to the temperature stability of trapped charge. However, the microscopic nature of the traps was merely inferred from macroscale x-ray diffraction. Also, it was not clear how much the specific proposed traps contributed to the total charge density, if that density correlated to crystallinity, and if the corona-charging was performed before or after crystallinity modifications (Ref. 31). In another study, incorporation of 1 wt% powdered magnesium stearate nucleating agent into PP electret fiber filters modestly improved baseline FE of electret filters from ~92.5 to 96 percent. This was attributed to increased amorphous-crystalline interfaces since there was an observed increase in polymer crystallinity (Ref. 27). Conceivably, additional understanding of storage mechanisms might be possessed by the research and development arms of the major manufacturers of electret filters. It has been said that the identities of their additives tend to be held as highly proprietary trade secrets (Ref. 15).

However, the open literature does contain some high-level descriptions of the nature of and methodology for analyzing the trapping states (Ref. 32). For example, it is thought that there can be three different types of trapping sites: Coulomb attractive sites, Coulomb repulsive sites, and neutral sites (Ref. 26). With data from thermally stimulated current (TSC) spectroscopy, it is then possible to make estimates of various parameters describing the trapping states using the Garlick-Gibson method (Refs. 26 and 33), which is consistent with a simple Arrhenius model for the trapped charge lifetime, as has been assumed elsewhere (Ref. 25). Parameters include the activation energy (W) for charge release (i.e., detrapping), capture area, relaxation time, and frequency of escape attempts. This frequency can vary by several orders of magnitude, from 10^8 to 10^9 s^{-1} to 10^{13} to 10^{14} s^{-1} for "strong" and "weak" trapping, respectively (Refs. 26 and 34). It has been supposed that detrapping of charges may occur by escape into the conduction band of the polymer (Refs. 8 and 35).

Obviously, such models reflect the fact that the charged state of electrets is metastable, and decay over time is expected. Therefore, the long-term durability of trapped charge and the kinetics of its discharge is a matter of significant practical importance for electret filters. Relaxation times of thousands of years have been reported for wax electrets (Ref. 16). As previously mentioned, N95 masks can retain their charge and specification performance for many years if stored properly. In a seemingly relevant study (Ref. 26), the relaxation time was calculated to be 1.0 year using the aforementioned method (Ref. 33) for the analysis of trap states in melt-spun and corona-charged PP-fiber filters. There it was found that Coulomb repulsive sites with W = 0.65 eV and neutral sites with $W \approx 1.0$ eV both existed and exhibited "strong" trapping. The former was attributed to interfacial trapping sites like those involved in Maxwell-Wagner polarization (i.e., where charges build up at interfaces corresponding to discontinuities in material electrical properties), is associated with lower temperature (30 to 50 °C) relaxation, and was found to almost fully dissipate after 60 days of storage time. Analysis of the higher energy neutral sites was based on relaxations observed near and at the PP melting phase transition (160 to 180 °C). These sites were primarily associated with the trapping of negative charge carriers injected by corona discharge, and to a lesser extent, inherent charge carriers of the PP material, which were thought to be mostly positive. In between the temperatures associated with the aforementioned site types, there was a third TSC peak at medium temperature with highly variable shape. It typically spanned 60 to 150 °C, was attributed to inherent and injected charge carriers, and values of trapping state parameters were not reported. This peak, like the higher temperature TSC peak, exhibited almost no change after 60 days of storage (Ref. 26).

Effects of elevated temperature and humidity during storage have also been investigated on meltblown corona-charged PP-fiber filters. Temperature of 120 °C for 48 h was found to cause reductions to the filtration performance and surface electric potential that were modest and significant, respectively (Ref. 8). In the same study, 90 percent relative humidity (RH) at 25 °C did not have a statistically significant effect on either surface potential or FE. In a different study, storage for 18 days at 24 °C at elevated RH ranging from 39 to 94 percent reduced the surface electric potential by ~30 and ~70 percent, respectively, as well as the charge lifetime, which dropped from its initial value of 1.8 years to 1.3 and 1.0 years, respectively (Ref. 35). However, in that study the corresponding effect on FE was not directly measured.

1.4 Potential Mechanisms of N95 Performance Loss During Long-Term Usage

Performance degradation of electret filters with time is generally different when they are being used compared to when they are passively exposed to air during storage. During active filtering, when such filters are "challenged" by aerosols and become "loaded" with captured aerosol particles, their FE changes in response to interactions with those particles. The literature indicates that complete electrostatic discharge of a filter is possible via aerosol loading (Refs. 6 and 13). However, the loading response depends on the type of aerosol and its characteristics, (size, charge, material, and physical state) (Ref. 36). For NaCl aerosols, the sign of change to N95 FE during loading depends on the RH (Ref. 37). Loading with oil aerosols reduces electret filter FE performance (Ref. 36) to such a severe extent that R- and P-class respirators are recommended rather than N95s (Ref. 38). Indeed, the "N" in N95 means "not resistant to oils." Yet, oil could be a relevant risk for N95 usage particularly in dense urban areas because lubricating oil has been found to dominate primary organic aerosol emissions from motor vehicles (Ref. 39).

Loading with solid particulate aerosols may reduce FE as well. In one study, challenge aerosols of various industrial dusts and fumes, as well as ammonium chloride salt, were tested with four different types of electrostatic filter materials (Ref. 40). In all combinations of filter and aerosol, the penetration increased with continued loading, that is, continued exposure to the test aerosol (Ref. 40). Loading the filter materials caused penetration to increase from ~1 percent up to final values ranging from ~3 to ~50 percent depending on the challenge aerosol. For ammonium chloride salt, the final penetration was ~15 percent after a ~1.9 mg/cm^2 cumulative loading on the filter (Ref. 40). During loading of N95s with a standard test aerosol (NaCl) in high humidity, penetration increases were measurable after just 2 h and were threefold changes at the final test point of 6 h for some test conditions, for example, larger particle sizes (Ref. 37). Compared to standard NaCl control testing, combustion particles like smoke from burning materials have also been found to have increased penetration through N95s and this was attributed to degradation of fiber electret charge (Ref. 41). As penetration depends on the type of smoke (Ref. 42), this effect might be pertinent to N95s being used for additional protection needs unrelated to COVID–19, for example, during the September 2020 wildfires in the western United States (Ref. 43).

The possible mechanisms of electret filter performance degradation with loading have also been discussed. For solid particulate aerosols, these include neutralization of the charges on the fibers by opposite charges on the incoming captured particles and dielectric screening of the charged fibers by said adhered particles (Ref. 6). Such mechanisms are thought to be active with oil aerosols as well, which may spread out into dielectric coatings on the fiber surfaces (Ref. 36). However, modeling of the neutralization mechanism was found to significantly underpredict performance loss, and so it is also thought that ionic conduction of impurities, which need only be present at a level of one part per million or more in the oil films, also contributes to FE losses via electret charge depletion (Ref. 36).

Although loading by solid particulates can degrade FE via weakening of the electrostatic mechanism, it is also possible for them to ultimately increase the lab-measured FE after a transient reduction. The reduction is probably caused by loading interfering with electrostatic capture as previously described. The mechanism of the ultimate increase is improved mechanical filtration, which may result from the solid particles clogging the filter and forming a filter cake (Ref. 44), having an overriding effect. This can happen with NaCl salt aerosols, thereby causing an adverse increase of the pressure drop (Ref. 44) if the air is sufficiently dry (Ref. 37). One pertinent example (Ref. 44) is from a test on a 3M PP blown microfiber filter where a NaCl aerosol challenge caused penetration to increase slightly from ~0.8 percent to just over 1 percent during the first 80 mg and then ultimately decrease to ~0.3 percent after 200 mg total loading. Afterwards, the pressure drop had increased by about threefold or possibly more, that is, from 7 to some unspecified value above 20 mm H_2O. In another study (Ref. 13), 5 mg/m^3 upstream loading of an electrostatically spun filter with a fine (10 to 200 nm) NaCl aerosol reduced FE during the first 10 h down to the levels of a discharged filter, for example, from ~85 percent down to ~20 percent FE at ~100-nm particle size. But further subsequent loading up through 140 cumulative hours then caused efficiency to increase back to approximately the same as that initially measured while at the same time increasing the pressure drop by a factor of 125.

The data of other experiments showed that the rate of pressure-drop increase rose with solid-particulate loading time for both advanced-electret and blown-microfiber media (Ref. 44).

While higher pressure drop due to mask clogging can have a positive impact on FE during a laboratory test, it may not translate to increased filtration efficacy of N95 masks during real-life application. According to a 2013 discussion of the literature, most particles penetrating N95 masks enter through air leaking around imperfections in the seal around the user's face (which may be exacerbated by repeated donning, Ref. 45) rather than passage through the filter (Ref. 46). If the mask pressure drop increased, such face seal leakage would become increasingly preferred as the path of least resistance. Therefore, the development of a large pressure drop in a mask could in fact reduce user protection. This is especially true if the breathability of the mask becomes so poor that a decision is made to stop using it.

Such decisions may be spurred by the user discomfort associated with wearing a mask with a large pressure drop. Indeed, N95s have been regarded by nurses (Ref. 47) and others (Ref. 48) as making it difficult to breathe and causing a perceived shortness of air (Ref. 47). In one study of healthcare workers wearing masks for full shifts, 71 and 23.6 percent of respondents experienced headaches and impaired cognition (Ref. 49), respectively. In another, there were complaints of lightheadedness, significant increases of blood CO_2 levels, and 22 percent of N95 removals were due to discomfort (Ref. 47). This study also highlighted other adverse effects of long-term mask use such as acne, which occurred in more than half of the participants (Ref. 49) and may be caused by buildup of natural facial oil on the skin and perhaps also on the mask.

In summary, there appear to be a number of ways by which N95 masks could be adversely impacted as a result of the extensive long-term reuse (e.g., occurring across multiple venues of living) that may be expected during a pandemic shortage. Loading in high humidity or by some aerosols including oils and smoke can be expected to reduce FE of the filter layers due to a loss of filter electrical charge, which is critical to FE. Notably, this may apply for lubricating oil, which is the dominant organic aerosol emission of automobiles. Clogging by particulates may be expected to increase the pressure drop of a mask and this in turn could lead to a reduction in its effective filtration efficacy via increased face seal leakage, thus reducing user protection. Clogging may also increase user discomfort, which sometimes is great enough to motivate mask removal. Finally, a buildup of natural facial oil could plausibly (1) lead to contamination of the filter layer with a corresponding loss of charge and performance or (2) cause user acne and reduce motivation to wear the mask.

1.5 N95 Decontamination Techniques Not Addressing Loading-Induced Performance Loss

Despite the clear importance of the issues noted, limited work has been done to address them in the development of techniques for N95 mask decontamination and reuse. Understandably, disinfection of the pandemic virus while maintaining FE has been a high priority. The Center for Disease Control (CDC) does not approve routine decontamination as a conventional standard of care, but in times of crisis (known shortage), they have recognized several techniques that have done well in this regard. These include ultraviolet germicidal irradiation (UVGI), vaporous hydrogen peroxide (VHP), and moist heat up (15 to 30 min at 60 °C and 80 percent RH) as the most promising methods to be used (Ref. 50). After VHP was approved, there was a report that the process resulted in mask degradation after only two to three cycles and the manufacturer had only confirmed it for up to four cycles of sterilization and reuse (Ref. 51). However, subsequent testing of VHP decontamination found good performance out to five cycles (Ref. 52).

Other decontamination techniques have also showed promise. Researchers at NASA Glenn Research Center and University Hospital in Cleveland, Ohio, have developed techniques using atomic oxygen and gaseous peracetic acid, respectively (Ref. 53). A team at the University of Illinois has identified dry heat (~20 min at ~100 °C, 50 min total heating time) using a common household electric cooker to be an effective means of sanitizing N95s while maintaining FE above 95 percent (Ref. 54). Although other testing also found good results with decontamination based on dry heat (Refs. 52 and 55), such a method may be risky if not performed correctly. Researchers, including the inventor of N95 masks, similarly proposed 60 min at 70 °C in an oven while hanging the mask with a plastic or wooden clip because if a mask contacts or comes within ~150 mm of hot metal, severe charge loss is possible (Ref. 56). Besides proposing a simple 3- to 4-day wait period to provide for COVID–19 neutralization prior to reuse, those authors also reported that 5 min of water boiling or steaming could be used to sanitize and resulted in performance that was under the 95 percent specification by only a few percent. This is consistent with the CDC's recognition of steaming along with liquid hydrogen peroxide (LHP) soaking (Refs. 3 and 57) as promising methods (Ref. 58). A comprehensive list of the results for different N95 decontamination techniques is available at Reference 59.

Although many of these sanitizing processes do a good job of maintaining FE, they were typically proven out via cyclic processing on virgin masks never used by a person. We are not aware of any decontamination method that was (1) validated

with testing of heavily used masks or (2) demonstrated to provide a like-new pressure drop for masks loaded by real-life long-term use. Thus, although many sanitizing processes have been shown to have minimal effect on the performance of as-received masks, it appears that none of them have been proven to alleviate any of the anticipatable adverse impacts to masks plausibly caused by extensive reuse, which were previously described in Section 1.4. None of these processes can be expected to restore use-induced losses to electrical charge and corresponding FE. Most of these processes are unlikely to (1) clean away oils that may degrade electric charge and/or irritate the skin or (2) remove clogged particles that may increase breathing resistance and amplify face seal leakage and user discomfort. Of the aforementioned methods, only atomic oxygen seems likely to have a good chance of success in these regards. Dry heat, moist heat, UVGI, VHP, LHP, vaporous acetic acid, steaming, boiling water, and especially 3 to 4 day waits all seem unlikely to remove oil and particles and restore the pressure drop of mask with clogged porosity. Water, to which hydrogen peroxide converts, has high surface energy (73 mJ/m^2) (Refs. 60 and 61), thus, does not effectively wet the filter fibers, which have low surface energy (27.2 to 32.6 mJ/m^2) (Ref. 8). Moreover, water without any detergent is obviously not particularly effective at removing fine particles or oils from fabrics.

1.6 Possible Path to Fully Restoring N95 Performance: Liquid-Based Decontamination and Declogging Followed by Recharging

In contrast, N95 sanitizing methods such as rinsing or soaking in soapy water or isopropanol are more likely to be able to remove loaded particles and oils from mask filter fibers, which could result from long-term use. The liquids of these sanitizing methods have lower surface energy, about 20 to 30 mJ/m^2 and 22 mJ/m^2, respectively (Refs. 60 and 61). Therefore, they should exhibit greater wetting on both the fibers and loaded particles and have more capability to remove the latter. Loaded oil would also be susceptible to removal due to surfactant action and solubility, respectively. Thus, these methods perhaps along with some gentle agitation may have the best chance to simultaneously sanitize and restore the pressure drop of masks. As noted by others (Ref. 62), these methods could also be expected to effectively neutralize the virus SARS-CoV–2 that causes COVID–19 by dissolving its lipid layer.

Unfortunately, washes with soapy water and isopropanol have also been shown to significantly reduce the FE of masks (Ref. 3) and are thus disfavored (Refs. 56 and 58). It is now well known (Ref. 15) that liquid isopropanol (Refs. 14 and 56) and liquid ethanol (Refs. 8 and 63) “erase” charge on PP electret fibers. It has also been reasoned that the surfactant in soapy water similarly has an adverse effect on the charge (Ref. 3).

If an effective recharging technique existed, such simple washes might be sufficient in complement. More broadly, a viable recharging method would relax a major constraint (i.e., retention of electret charge) on the approach to the decontamination. Mask decontamination could then be expanded into a more complete rejuvenation process that further includes restoration of the pressure drop and any FE losses. Such a process would then allow for higher effectiveness and longer useful lifetimes for reused masks.

The physical mechanism by which a small concentration of soap causes relatively harmless liquid water to erase charge from electret fibers has not been established as far as we know. It has been demonstrated that water droplets may acquire excess electric charge from high-voltage metal surfaces (Ref. 64), which they easily wet. Therefore, it might be that enhanced wetting on the fibers provided for by the soap-reduced liquid surface tension is the key to aqueous charge escape from the electret fibers. One can imagine that unipolar charges that escape into a liquid could lower their energy by spreading out throughout said liquid and thereby reduce their repulsive interactions. This is straightforward for a liquid bath, and also seems to apply to a fiber body whose cylindrical diameter is increased slightly by a thin layer of wetted water (which also offers dielectric screening). Also, the excess charges might be stabilized by water molecules in different spatial configurations, so there could be a significant microconfigurational entropic impetus that is similar to that for a solute dissolving into solution. The liquid could also offer a path for electrical discharge to ground if the liquid and contacting-solid materials are not good electrical insulators. The physical barrier to entering a liquid for a charge trapped on a polymer surface should be significantly higher in energy and/or larger in physical distance if wetting is absent. Conversely, intimate contact of the polymer-fiber surface with a wetted liquid could facilitate quantum tunneling of the charge into the liquid and thereby obviate detrapping occurring by thermal excitation into the conduction band of the polymer. It has been noted that trapped charges in polymer electrets are stabilized by their molecular environment (Ref. 25), and in this view, charges trapped at a bare polymer-air interface would seem to be destabilized by a wetted liquid that offers one or more energetically favorable alternative states. These arguments also seem consistent with degradation of polymer electrets by liquid but not gaseous ethanol (Ref. 63) and xylene (Ref. 65) as well as liquid-oil wetting of electret filter fibers (Ref. 36). The standard test oil for challenging filters, dioctyl phthalate, has an extremely low surface energy (Ref. 66) (15 mJ/m^2), and thus can be expected to exhibit extremely high wetting. Loading with droplets of a different oil with a much higher surface energy (Ref. 67) of 33 mJ/m^2 also caused degradation and was found to

spread out on spun-type electret filter fibers (Ref. 36). This result provides some context for lubricating oils that have a surface energy of 25 to 35 mJ/m^2 (Ref. 60) and were previously mentioned as a possible risk from automobile emissions (Ref. 39).

There is some precedent for recharging after discharging with liquid alcohol or in water with a detergent. In one study, a triboelectrified needled felt had its initial FE of 97.8 percent reduced to 20 percent by washing with isopropyl alcohol and was subsequently recharged to 82 percent efficiency via corona discharge (Ref. 14). In two other studies that were published after the experiments described in this report were conducted, recharging of N95 masks was explored (Refs. 62 and 68). In the first, the as-measured FE was apparently restored by recharging N95 masks for 60 min after discharging via alcohol or laundering in a washing machine (Ref. 62). Although this was a meritorious effort, the reported FE values were based on 300-nm challenge particles, which could be expected to yield higher FE values than those associated with the most penetrating particle size that is typically around 50 nm (Ref. 2). In the other study (Ref. 68), which was also commendable, N95 masks were laundered with detergent and color bleach and then subsequently recharged with a Van de Graaff generator and measured for FE using 300- to 500-nm challenge particles in a 20-second test. This increased the apparent FE from 72 ± 17 percent (after washing) to 94 ± 4 percent, but the large challenge-particle sizes and short filtration-test times leave questions about the extent, size dependence, and long-term durability of the restored performance. The result of a single trial described in the present report seems relevant to the latter characteristic and is described in the final paragraph of Section 3.4.

Still, the latter efforts (Refs. 62 and 68) to recharge entire N95 masks are particularly noteworthy because the overall electric potential of a mask is generally subject to influence from nonactive components (which may hold a transient static charge) in addition to its active filter layer whose charged state should be quasi-permanent. Nonactive components include rubber straps, metal parts (e.g., nose clips and strap staples), a stiff layer to maintain mask shape, an outer uncharged cover layer, and for some variants, an exhalation valve or a biological-liquid barrier layer. The presence of these components and the shapes of N95 masks (which vary across manufacturers, models, and used masks from different-user faces) could plausibly affect the distribution of electric fields and thereby complicate attempts to uniformly recharge the filter media. Therefore, in the present study, it was thought that an appropriate first step would be the development of a recharging technique for standalone coupons of N95 filter media after being discharged with alcohol or soapy water. Once that was done, the more complex problem for a full N95 mask would be pursued.

1.7 Practical Considerations for Process Deployment During Pandemic

Scalability is a major consideration in a pandemic scenario. For a viable N95 restoration process, the variations in N95 design noted previously are one factor that affect this. To assess scalability of a given approach, it is critical to first establish the minimum requirements for the outcomes that make a process worthy of deployment. Such requirements should probably be based on (1) the fact that the degree of performance degradation of a given used mask would depend on the extent of exposure to the aforementioned mechanisms and is generally unknown and (2) the notion that the process should always improve or at least not harm mask performance. In regard to initial FE, a relatively conservative requirement is that the recharging process should result in FE ≥ 95 percent. An even more conservative requirement would be that recharging results in FE ≥ 99 percent since new N95s sometimes perform at that level (see Refs. 2 and 3). However, such requirements might be justifiably relaxed if (1) new understanding resulted in mask performance becoming a predictable function of long-term usage time or (2) a highly scalable and complementary performance evaluation technique for used masks was developed. Other requirements should address the pressure drop, performance during long-term loading, and maintenance of face seal (which depends on the N95 shape, nose clip, and the potentially replaceable straps).

For a scalable recharging process, the time required per mask, availability of processing resources, operator safety, and process repeatability are some of the important considerations. The mask recharging time of 60 min demonstrated by one group (Ref. 62) may or may not be scalable. Also, their process employed high and repeatable voltages with a direct current power supply. However, use of such a power source amounts to operator safety risk that is detrimental to scalability. This was noted by another investigator whose process employed a safer Van de Graaff generator as well as a shorter and more scalable 3-min mask recharging time (Ref. 68). Such generators are safer despite extremely high voltages because they produce miniscule currents and are more scalable in that regard. As they could be sourced from physics classrooms, they might also have improved availability, but repeatability factors might challenge their scalability. Namely, recharging results from Van de Graaff generators might vary due to differences in the output voltage associated with different model polarities and particulars of their designs, room RH, and the cleanliness of the generator components, which are prone to collecting dust and yet do not always respond well to cleaning (Ref. 69). An alternative charging process executable with a widely available commercial consumer ionic hair product might have high

scalability if the repeatability of results was high. If preceded by an appropriate wash in rubbing alcohol or soap and water for sanitization and successful declogging, such recharging could allow for a simple do-it-yourself mask restoration process with wide proliferation.

Another matter related to scalability is that at times during the COVID–19 pandemic, many governments have required community members to wear masks of any sort due to in large part the lack of available N95s, which was especially severe outside of the medical community. However, the efficacy of simple masks (nonrespirator, often made of cloth) has been broadly challenged especially in regard to their ability to protect the wearer (Refs. 70 and 71). Early in the COVID–19 pandemic, this spurred the decision of some people to not wear masks at all (Ref. 72). Therefore, the public might enjoy increased protection during a future pandemic aggravated by an N95 shortage if a method for improving the wearer protection of common-fabric facemask materials was available and could be performed by a layperson. Therefore, charging of such materials is an interesting topic for future research. Such research and the public-health impact of common-fabric facemasks might also be improved by leveraging recent efforts seeking to identify the best fabric materials and arrangements (Refs. 7 and 73). Yet, it should be noted that the modestly improved filtration performance that has so far been demonstrated after charging simple mask materials is substantially and grossly inferior to that of three-ply surgical masks and N95 masks, respectively.

2.0 Experimental

2.1 Sample Preparation

Coupons with a 2-in. (51-mm) diameter of nonwoven PP filter media were extracted from N95 masks (Figure 1(a) and (b)). Like the masks, these coupons had two plies of filter media. Coupon thicknesses were ~0.13 to ~0.25 mm when tightly squeezed by calipers. The box containing the masks suggested that they were produced during or before 1997.

Sometimes the dual-ply PP coupons separated. In such cases, the plies were placed back together and charged as a pair except in a few cases, which are specifically noted. Filtration testing of PP coupons always occurred as a dual-ply pair.

Unless otherwise noted, PP coupons were discharged prior to each recharging attempt. Alcohol exposure was the default means of discharge. On a few samples marked with “SW” nomenclature, soapy water was used to discharge.

Fabrics were also selected from a local store (Joann Fabrics and Crafts, North Olmsted, Ohio). Criteria for selection were minimal blending of weave materials, minimal light penetration through the weave, and white or off-white color to avoid the influence of obvious color dyes. The four fabrics chosen were 97 percent cotton and 3 percent spandex, 95 percent nylon and 5 percent spandex, 100 percent polyester #1721-9569, and 100 percent polyester #0074-0647. These were cut into 51-mm circles (Figure 1(c)). The two fabrics containing spandex had very tight weaves and minimal light penetration.

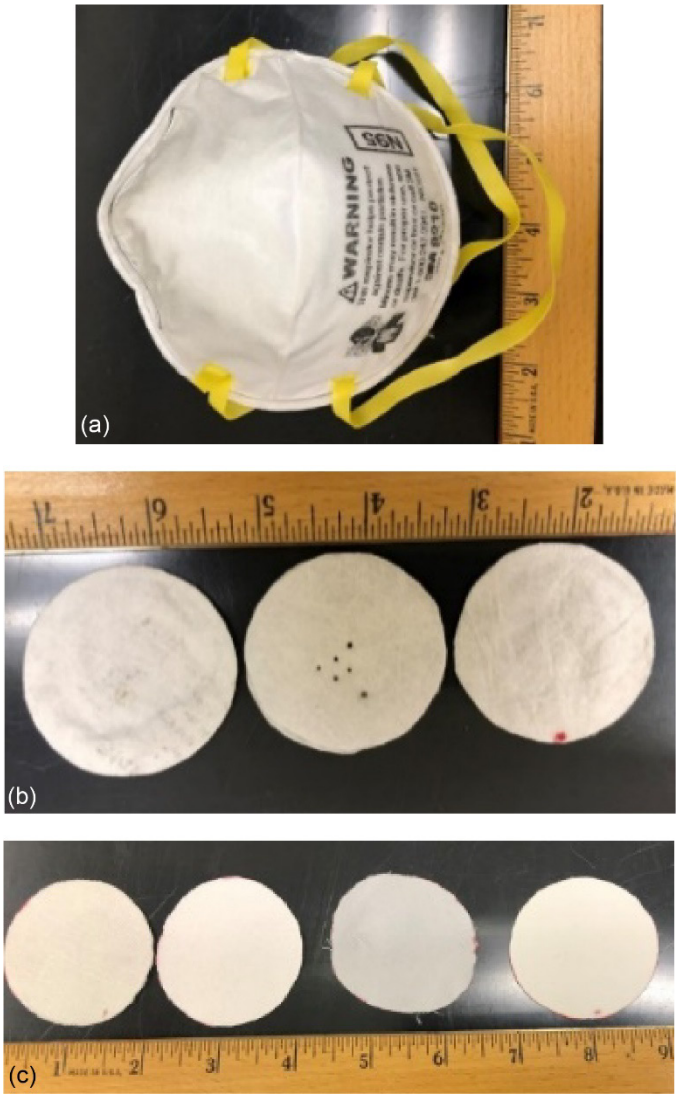

Figure 1.—Mask and filter coupons. (a) N95 mask. (b) Filter coupons extracted from N95 masks including one with pin holes developed from arcing during a charging attempt. Some coupons had small amount of light gray material on one surface due to bleedthrough of print on mask cover. (c) Coupons of other fabrics that underwent charging attempts. From left to right, 97 percent cotton and 3 percent spandex, 100 percent polyester #1721-9569, 100 percent polyester #0074-0647, and 95 percent nylon and 5 percent spandex.

2.2 Measurement of Surface Potential

Sample handling was conducted carefully and while wearing nitrile gloves to avoid depositing natural oils or transient (and presumably useless) triboelectric charge. A TAKK 5740 (TAKK Industries) static potential meter was used to measure the surface potential at the manufacturer-specified standoff distance of 4 in. (~100 mm) from samples. For this, a 100-mm ruler was put into place and then removed while a best effort was made to hold the 100-mm distance steady during measurement. The meter reading was typically recorded as a range reflecting the lowest and highest values observed. However, it should be recognized that the reported results, which correspond to 51-mm coupons, are probably not comparable to values in the literature measured on larger sheets due to differences in sample size. This static meter was also used to roughly gauge production of electrical ions by other equipment.

A similar SIMCO FMX-003 meter (Simco-Ion), which is the same model used in Reference 8, was also tried. However, it appeared that measurements by the handheld meters could have the effect of bleeding charge from charged samples, which lowered the magnitudes of readings. As a result, the SIMCO FMX-003 was abandoned because it appeared to interact too strongly with highly charged samples at its manufacturer-specified 1-in. (~25-mm) distance, and its readings are not reported. On a very limited number of occasions, TAKK readings were taken at a 25-mm distance in order to amplify the measured signal and verify the detection of a strong electric potential at a 100-mm distance.

Although mitigated by the larger 100-mm standoff, charge bleedoff also seemed to be possible with the TAKK meter. Therefore, surface potential measurements were sometimes not taken to avoid this effect, for example, when recharged coupon electrostatic movement was pronounced. An example of moderate electrostatic movement for recharged PP is shown in Video 1. Particularly strong movement sometimes manifested as coupon plies repelling each other and becoming tricky to handle as a coupled pair. When pinched together at a single point, such repulsion resulted in the repelling plies forming a "V" shape with up to ~50-mm maximum separation. Similarly, strongly recharged coupons would sometimes adhere to the top lid of the plastic container in defiance of gravity.

2.3 Charging Methods, Equipment, and Supplies

Experiments were made with different approaches to charging the coupons. These include trials based on custom corona discharge configurations as well as a limited number of attempts with consumer ionic hair products. The former group constituted the vast majority of the total.

Generally, PP coupons were recharged as a two-ply pair except in a few noted cases where the plies were recharged individually and then recombined for filtration test. Repeated attempts were made to recharge a given coupon because (1) FE test results for recharged coupons fell short of the 95 percent goal and (2) preservation of valuable N95 masks was prioritized over rigid maintenance of equivalent thermal-electrical history of coupons. Coupons tended to be reused and undergo further recharge attempts until being unintentionally damaged, for example, by excessive local heating. Recharging of a given coupon was usually discontinued if it showed signs of any melting, such as pinholes from arcing. In two cases where there were two pinholes or fewer, holes were sealed shut via careful application of glue with a hot glue gun in order to conduct a final filtration measurement before retiring the coupon.

Various equipment and parts were used for producing or routing airflows during charging experiments. These are shown in Figure 2. They included two Volare® V1 ionic hair dryers (BaBylissPRO®), a Poniie PN-H20 heat gun that was programmable to 10 °F (~5.6 °C) increments, an AC Infinity Cloudline S6 (model AI-CLS6) variable speed fan with eight speed settings, high-temperature rubber hoses, and three-dimensional- (3D-) printed adapters. A Yamato Scientific America, Inc., DKN302C drying oven or a manually constructed temperature cell were also sometimes used for temperature control during charging. Cooling of materials after hot charging was performed with different methods, which are noted throughout the report. Besides the fan, laboratory compressed air and cold nitrogen gas released from a liquid nitrogen dewar (not shown) were also tried.

2.3.1 Method Class 1—Charging by Custom-Designed Corona Discharge Configurations

The custom corona discharges all used a negative-biased high-voltage emitter point source in a variety of different configurations relative to surrounding materials, for example, a counter electrode with a 2-in. (51-mm) diameter. The different setups were used to test different approaches to controlling the applied electric field, temperature, and cooling of the sample. Since samples were circular with a 51-mm diameter, such configurations were designed with the intention of achieving an axis of symmetry from the corona emitter to the counter electrode and a cone-shaped electric field distribution. In most cases, the sample was positioned close to or in contact with the equivalent-diameter counter electrode, and therefore, the electric field on the sample was thought to have been relatively uniform.

Figure 2.—Equipment used to produce forced air during charging experiments. (a) Fan used for cooling, Volare® ionic hair dryers (BaBylissPRO®), and Poniie temperature-programmable heat gun. (b) Adapters and high-temperature tubing used for directing airflows. (c) Adapters connected to forced-air equipment. (d) Dual-stream merging adapter connected to twin ionic hair dryers

The fundamental features of the various configurations that were tried are shown in the schematic diagrams of Figure 3. Namely, they show how the sample was positioned relative to the high-voltage emitter and steel disk counter electrode, which was used in nearly all cases, as well as whether or not this counter electrode was electrically grounded or "floating," that is, having no electrical connection. They also show the manner in which metal screens were sometimes used to contact the sample. The different configurations are named as follows:

- Individual Floating Disk (IFD)
- Floating Disk Stack (FDS)
- Floating Screen (FS)
- Floating Disk-Magnet Stack (FDMS)
- Grounded Disk-Magnet Stack (GDMS)
- Through Current (TC)
- Through Current with Emitter-Side Screen (TCES)
- Through Current with Ground-Side Screen (TCGS)
- Through Current with Emitter- and Ground-Side Screens (TCEGS)

The distance between the emitter and back plane of the sample (d_{emit}) and the distance between that plane and the electrically grounded counter electrode (d_{CE}) are defined. Some configurations may be seen to closely resemble each other from an electrical standpoint, namely IFD with FDS, IFD with FS,

and GDMS with TC in the case of d_{CE} = 0. The procedural details used with the various configurations evolved throughout the experimental work and are noted accordingly throughout Section 3.0. Photographs are also provided for some setups.

As indicated, sometimes a significant aspect of the configuration was a magnet. This was axially magnetized Grade N42 NdFeB with a 51-mm diameter, 3.18-mm thickness, 128-N pull force to a contacted steel plate, and a Ni-Cu-Ni coating. In some other instances, the sample was contacted with a metal screen of one of two types. One type of screen was thin and relatively flexible. Caliper measurements indicated wire thickness, planar thickness, and inner-square edge distances of about 0.18, 0.43 to 0.46, and 1.3 to 1.5 mm, respectively. The other type of screen was thicker and stiffer, and the corresponding values were 0.30, 0.71 to 0.76, and ~1.02 mm, respectively.

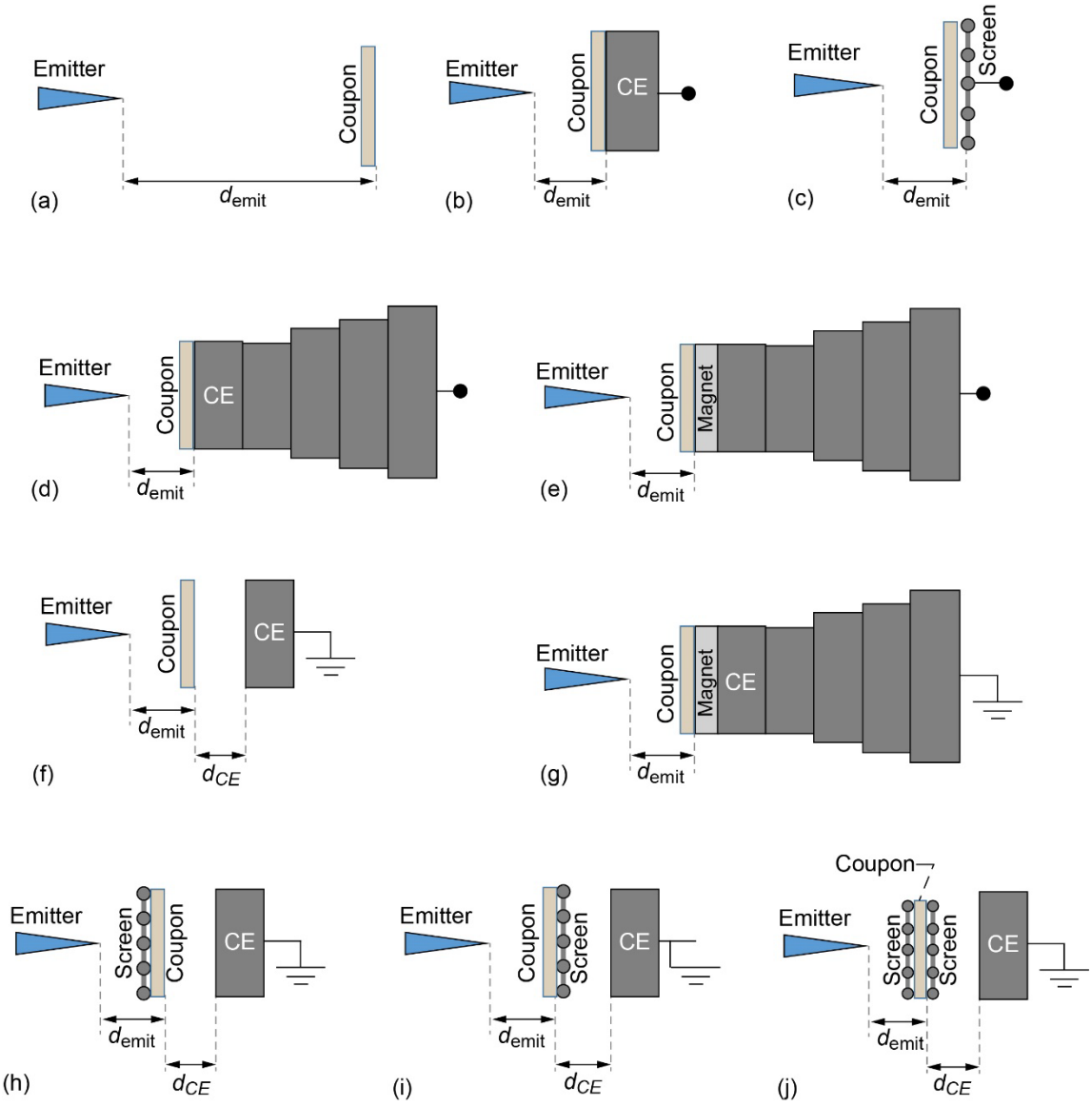

Figure 3.—Different electrode configurations that employ custom setup corona discharge with high-voltage emitter and counter electrode (CE). (a) Floating Coupon (FC). (b) Individual Floating Disk (IFD). (c) Floating Screen (FS). (d) Floating Disk Stack (FDS). (e) Floating Disk-Magnet Stack (FDMS). (f) Through Current (TC). (g) Grounded Disk-Magnet Stack (GDMS). (h) Through Current with Emitter-Side Screen (TCES). (i) Through Current with Ground-Side Screen (TCGS). (j) Through Current with Emitter- and Ground-Side Screens (TCEGS). Distance between emitter and back plane of sample (d_{emit}) and distance between that plane and electrically grounded CE (d_{CE}) are defined.

Most charging attempts made use of one or more thermoplastic fixtures and widgets, which were custom designed and 3D printed. These include different generations of a sample holder and electrode holder (Figure 4) along with accessory parts and the aforementioned 3D-printed adapters for routing airflows. These enabled or supported many of the configurations that relied on the previously described symmetry and some type of corona discharge process. For example, there were retainer rings and clips for holding or manipulating the test sample and heat shields for ensuring that the plastic used did not melt from a highly directed flux of hot air. All generations of the sample holder and electrode holder had a 51-mm borehole. Samples were held along the outer 3.18 mm of their perimeter by a gripping portion of the sample holder that had a ring shape and total thickness of 4.06 mm, that is, including the retainer ring. Altogether these features provided a 44.5-mm-diameter opening for unobstructed exposure of the central portion of the sample to the applied electric field.

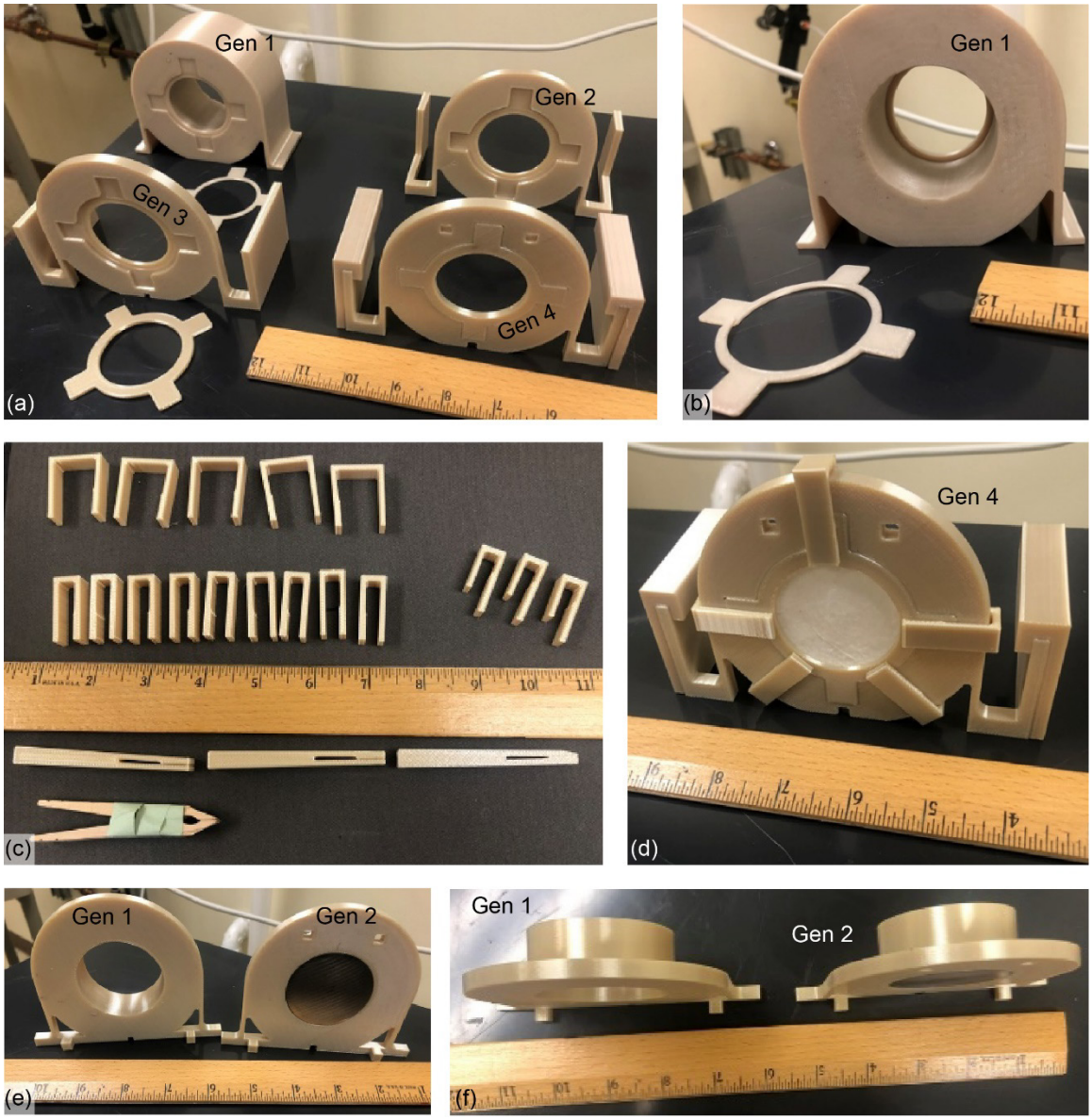

Figure 4.—Custom parts associated with holding filter coupons and metal-disk electrodes. Different parts were used for different charging methods. (a) Frontside views of different-generation sample holders (Gen 1, Gen 2, Gen 3, and Gen 4) along with retainer rings. Gen 4 has heat shields and retainer ring attached. (b) Gen 1 sample holder backside and retainer ring. (c) Clips used in some configurations to forcefully grip retainer rings, metal-disk electrodes, and filter coupons. (d) Gen 4 sample holder with clips gripping onto retainer ring to help hold filter coupon in place. (e) Front view of Gen 1 and Gen 2 electrode holders. (f) Top view of Gen 1 and Gen 2 electrode holders.

The 3D-printed parts were made from stock material produced by Stratasys, Inc. (Eden Prairie, Minnesota). Nearly all parts were Ultem® 9085 material for which the heat deflection temperature (HDT), glass transition temperature, dielectric constant, dissipation factor, strength, and volume resistivity were 153 °C, 186 °C, 3.0 to 3.2, 0.0026 to 0.0027, 4.3 to 11.4 kV/mm, and (4.9 to 8.2)×10^{15} Ω·cm according to manufacturer specification. However, some parts were printed with polyphenylsulfone (PPSF) for which the values were 189 °C, 230 °C, 3.0 to 3.2, 0.0015 to 0.0011, 11.0 to 11.4 kV/mm, and (5 to 15)×10^{13} Ω·cm, respectively. These parts included the Gen 1 sample holder and heat shields, which also improved the stability of Gen 2, 3, and 4 sample holders by altering the center of mass.

A negative polarity Van de Graaff generator (Lethan Corporation, Model LC2910-HC, nominally –325 kV) was used as a high-voltage source. Emitters used included an old LaB_6 crystal from a JEOL 840 scanning electron microscope Denka cathode (Denka Company Limited), a 4.76-mm-diameter 7075 aluminum alloy pin with tip fashioned into a rough dome shape by manual grinding, and a stainless steel needle with a 1.8-mm diameter. The LaB_6 work function is ~2.7 eV, and the 7075 composition was selected because the photoelectric work functions of Al and its major alloying elements Zn and Mg are relatively low compared to many of the more stable elemental metals (Ref. 74). Respectively, the values are 4.06 to 4.26, 3.63, and 3.66 eV, and there is literature suggesting that the work functions of metal alloys follow fairly well-behaved mixing rules (e.g., Al) (Ref. 75) and may be lowered by alloying with a small amount of different metal with a lower work function (Ref. 76).

Temperature measurement was performed with a K-type thermocouple or Extech infrared laser thermometer (model 42510A; FLIR Systems) using an emissivity value of 0.97 for N95 filter coupons (corresponding to PP) and 0.92 with polytetrafluoroethylene (PTFE) sheets for temperature checks.

2.3.2 Method Class 2—Charging Methods Using Ionic Hair Products

Some commercial off-the-shelf ionic hair products were also tried as means of charging materials since these could potentially allow for wide-scale deployment of methods if successful. Corona discharge may have also been a mechanism employed by some of these products, which were found to produce ionized air. The most notable of these was an ionic hair dryer, that is, the high-powered (2,000 W) BaBylissPRO® Volare® V1 ionic dryer that utilizes a Ferrari-designed engine and a triport ionic generator. This device can operate at low or high air velocity with any of three different air temperature settings (room temperature, warm, or hot). The nozzle inner and outer diameters are 35.3 and 41.7 mm, respectively. Its production of a strong flux of negative ions during warm and hot operation was confirmed by the static meter rapidly overloading to beyond –200 kV shortly after being impacted by the airflow. This is demonstrated in Video 2.

2.3.2.1 Charging With Volare® V1 Ionic Hair Dryer

The fundamental feature of this was directing hot ionized air through the circular area of the 51-mm-diameter filter coupons. However, a number of variants on the configuration and method were tried with this charging procedure. These are all shown in Figure 5. In all variants, the sample was held by the first-generation sample holder. The retaining ring was affixed with high-temperature tape. Unless otherwise noted, the highest settings were used for the ionic-dryer velocity and temperature. A thermocouple was not used to measure coupon temperature due to concerns over its impact on the electric field distribution.

In the original configuration (Ionic-Dryer Arrangement 1), the hot ionized air was directed to and passed through the sample and borehole of the first-generation sample holder unimpeded. During such charging, the flow of hot ionized air and infrared (IR) thermometer laser spot were manually centered on the filter simultaneously with a two-handed approach to monitor the coupon temperature. After heating up, the filter temperature was maintained at the target temperature for the cited time manually via a best effort. After accumulating the target time, heating was ceased, and the holder was rapidly moved in front of the fan at 6/8 speed for ~60 seconds of cooling via forced air on the filter coupon.

In subsequent trials, there were problems with sample melting from nonuniform heat flux and the retaining ring failed to hold the sample against the strong airflow. This resulted in the sample flying out of the holder into the air prior to achievement of longer targeted charging times and may have been due to wear of the 3D-printed plastic. Clamping the retaining ring with C-clamps did not solve the problem.

Therefore, a variant configuration (Ionic-Dryer Arrangement 2) in which the sample could not fly away was developed. This employed a barrier, which was made of balsa wood (3.18 mm thick) and secured on top of a steel disk (51-mm diam., 25 mm thick) with high-temperature tape. This assemblage was then placed on top of a 50-mm-thick steel plate that was electrically grounded. The filter coupon was then clamped via retaining ring into the sample holder and that assembly was then placed coupon-side down on top of the barrier stack. In this way, the coupon was positioned slightly above the barrier, which lay underneath the retainer ring. In this setup, the hot ionized forced air pushed the coupon against the barrier instead of ejecting it. The disk and grounded plate were intended to encourage negative ion flow through the coupon, and the wood spacer was intended to prevent discharge of the charging coupon to ground by avoiding direct contact. The barrier shape was far from a perfect

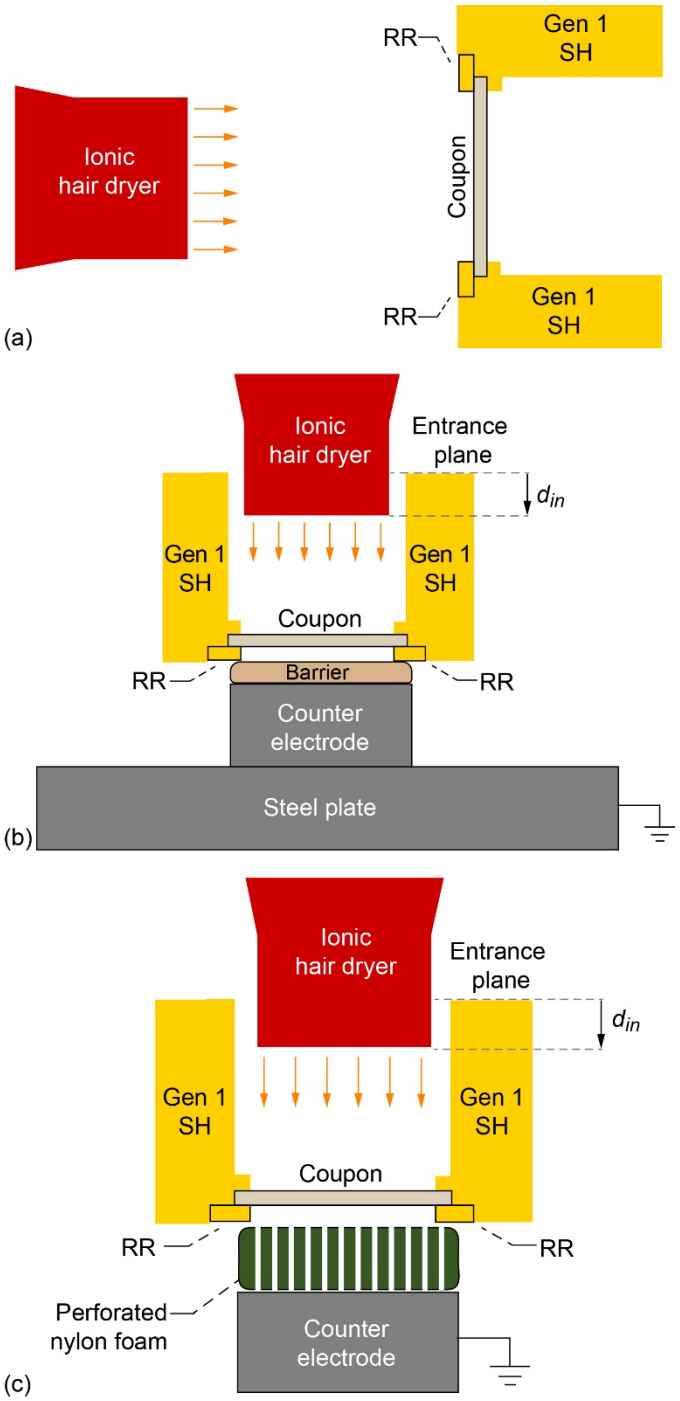

Figure 5.—Different configurations using ionic hair dryer as primary source of negative air ions. Described in Experimental section. All used Gen 1 sample holder (SH) with retainer ring (RR). Nozzle insertion depth (d_{in}) is defined relative to entrance plane to borehole on backside of Gen 1 SH. Positive and negative values of d_{in} define nozzle insertion and standoff, respectively. (a) Ionic-Dryer Arrangement 1. (b) Configuration for Ionic-Dryer Arrangements 2 and 3. (c) Ionic-Dryer Arrangement 4.

circle and allowed extensive leakage of air through the gap between the barrier and retainer ring. When the nozzle of the ionic dryer was very close to or inserted into the borehole of the sample holder, the process of heating up to the target temperature was periodically interrupted in order to move the IR thermometer laser spot onto the sample and thereby monitor its temperature. Such was also done during charging when the charging time at the target temperature exceeded 30 s. Alternatively, when a significant standoff distance from the borehole was used, the sample temperature was more or less continuously monitored during charging since the laser spot and hot ionized air could be directed onto the sample simultaneously.

A few other variant configurations were tried. In Ionic-Dryer Arrangement 3, the barrier is redefined to include a layer of 1.5-mm-thick PTFE on top of the balsa wood—the intent was to further reduce the likelihood of coupon discharge to electrical ground. In Ionic-Dryer Arrangement 4, the balsa wood and PTFE were removed and replaced with nylon foam that was 13 mm thick. Numerous holes were punched in this foam to promote flow of hot negative air ions through the filter to ground. This change also increased the distance between the filter coupon and electrical ground. Also, the large steel plate was discarded, and the metal grounding wire was attached more directly to the steel disk via a magnet.

2.3.2.2 Charging With Hair Straighteners

Four hair straighteners advertised to be able to impart charges to hair were also tried on a very limited basis. Two of these produced a flux of negative ions through the air via a point-source emitter near the base of the heated plates. These were the Pritech TA-1978 (Pritech Beauty Care), as well as the BabyLissPRO® Nano Titanium™ Prima3100™ 1-in. (25.4-mm) model (BLPNTP3100), which advertises IonMultiplier Technology. By using the static meter, this was confirmed for both and Video 3 shows a demonstration for the latter product. The Bio Ionic® OnePass 1-in. (25.4-mm) model and HTG model HT087 straightening irons were found to impart positive charge triboelectrically. The Bio Ionic® was advertised as having patented silicone strips and as being powered by a proprietary complex of natural minerals (NanoIonic™ MX). The HTG was advertised to employ both ceramic tourmaline plates and a negative ion generator; however, an ion stream was looked for but not detected by the static meter.

During treatment with the straighteners, samples were held with a double or triple nitrile-gloved hand while being stroked with the heating plates. When using a product employing an ion flux, the sample was held as close as possible to the point source. This process was then followed by a quick cooling via the fan at 6/8 power setting and ~25-mm (1-in.) distance.

2.4 Filtration Testing

Filtration efficiency (FE) testing of mask-media coupons was performed in accordance with industrial test standards. Tests on these filters were conducted using a TSI Incorporated fractional filter tester (Model 3160), which was available during the COVID–19 pandemic. The testing approach deviated from the NIOSH standard (Ref. 77) but was similar to that used in a recent study (Ref. 78) that cited results (Ref. 79) suggesting that the NIOSH test lacks sensitivity to nanoparticles smaller than 100 nm in size.

The TSI 3160 is a complete industrial filter test system employing the EN 1822 standard, parts 4 and 5, and is shown in the representative picture of Figure 6. This filter tester measures the pressure drop and particle penetration over a range of particle sizes. It generates NaCl salt crystal challenge aerosol, which was introduced into the airflow through a bank of injectors. Air is supplied through the building's pressurized service line, which is filtered and dried before entering the main test air line. Before the aerosol was introduced into the main flow, it entered a mobility classifier, which selectively allowed particles of a specific monodisperse size to pass through into the flow upstream of the test filter. Up to twenty specific monodisperse particle sizes can be chosen to cycle through during one test. Particle counts were measured upstream and downstream of the filter using condensing particle counters, providing measurements over a range from 15 to 800 nm.

A coupon holder was designed and fabricated in order to support a 51-mm-diameter cutout coupon in the tester's filter holder. Figure 7 shows an isometric computer-aided design (CAD) 3D drawing of the two sections of the holder assembly. The coupon holder assembly was made of two cylindrical sections with internal conic surfaces that converged to a 38.1-mm-diameter opening where the coupon was exposed to the flow. An initial prototype was made out of plastic via 3D printing, but this was set aside because the conic surface material retained a high level of electrostatic charge that could collect challenge particles and interfere with testing. The holder that was eventually used was machined out of aluminum. Although this metal holder might have contributed to charge bleeding off from recharged coupons, a rubber gasket was used in an attempt to mitigate that. Also, any recharged state that lacked robustness in such a way is not likely to be very useful.

During coupon testing, the flow rate was 7.2 LPM. This produced the same face velocity on a 51-mm coupon as on a mask at a rate of 85 LPM, which simulates an equivalent peak respiratory flow rate (Refs. 77 and 78). Some low-flow tests were also periodically conducted throughout testing to check for particle leakage. A test at 20-percent-rated flow should produce an order of magnitude drop in penetration.

Figure 6.—TSI Incorporated fractional filter tester (model TSI 3160).

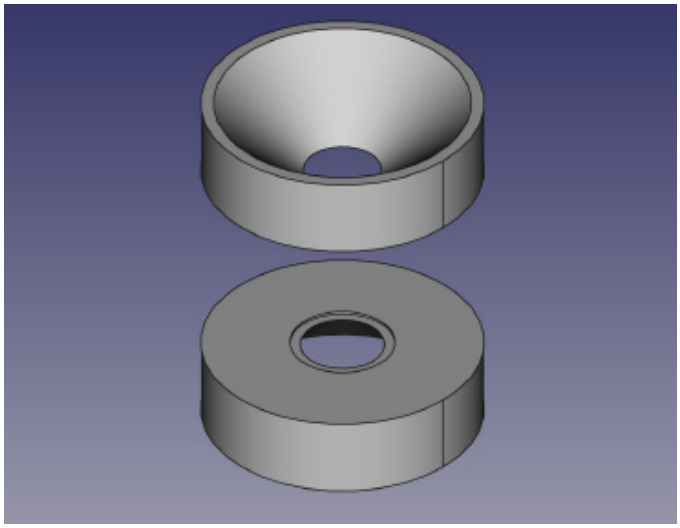

Figure 7.—Three-dimensional computer-aided design (CAD) drawing of coupon holder for filtration testing.

Instantaneous FE was determined and is reported at the most penetrating particle size. For each test, this was estimated from a penetration curve that was determined by curve fitting to measurement results at different particle sizes. The particle size range was 15 to 280 nm, and three to nine different sizes were

used depending on the test. Usually, a smaller number of different sizes was chosen due to the large number of coupons to be tested. For each coupon, at least three tests were conducted to statistically confirm the result. Throughout this report, FE is reported as the average of the test results. Table I to Table VI provide the standard deviations. The pressure drop of PP coupons was generally in the 4.4 to 7.1 mm H_2O range and was not significantly increased above that range by any of the recharging techniques except in a few noted cases.

Also, a limited number of loading tests were performed by running the software in a timed mode. In this mode, only one particle size could be selected for particle generation, and 91 nm was chosen. The sample filter was exposed to a steady concentration of particles of the specified particle size for the duration of the test. The software had an inherent time limit approaching an hour during a timed run. Therefore, one or two test runs of 52 to 54 min each were performed on the tested samples.

3.0 Results and Discussion

3.1 Baselines for As-Extracted N95 Filter Media

Filtration measurements of the as-extracted N95 material indicated that good performance had been retained even after ~23 years of storage. Results on different samples were FE = 95.5, 95.9, 95.3, and 93.4 percent. Loading testing was also conducted on one of the as-extracted PP samples. The results are available in Figure 8 in comparison to data from recharged coupons described later. The discontinuity in the trending of the pressure-drop data is a result of the stitching of two ~50-min datasets.

Yet, as-extracted samples usually did not exhibit significant electrostatic movement or surface potential. For example, the values for one sample ranged from +0.26 to +0.41 kV. These voltage magnitudes are quite low compared to values for recharged samples presented later. Rather than interpreting these low potentials to mean that the as-extracted N95 material possessed a low level of excess charge, it is supposed that it may have possessed a multitude of nearly counterbalanced opposite-sign charges resulting from bipolar charging (Ref. 24). Electric potential measurements of filter media extracted from as-received N95s of various manufacturers in another study, which were weak, not reproducible, or almost random in magnitude and polarity (Ref. 68) seem to be consistent with our results and bipolar-charged media. Another possibility might be transient (nonelectret) static surface charge (of limited or no value) masking the useful quasi-permanent electret charge, thereby convoluting the results of attempts to measure the latter. In the present study, N95 filter media was indeed found to be able to acquire transient static charges from intentional rubbing with nitrile gloves or peeling apart layers.

Some measurements of electrical potential were also executed on some whole N95 masks and their constituent components while suspended by strings during the mask breakdown process for coupon extraction. It was of interest to see if the charged filter media might dominate the electric potential of entire masks, and thus serve as the basis of a highly scalable mask-performance evaluation technique. This did not seem to be the case; the nonfilter components were found to strongly influence the electrical potential of the whole masks.

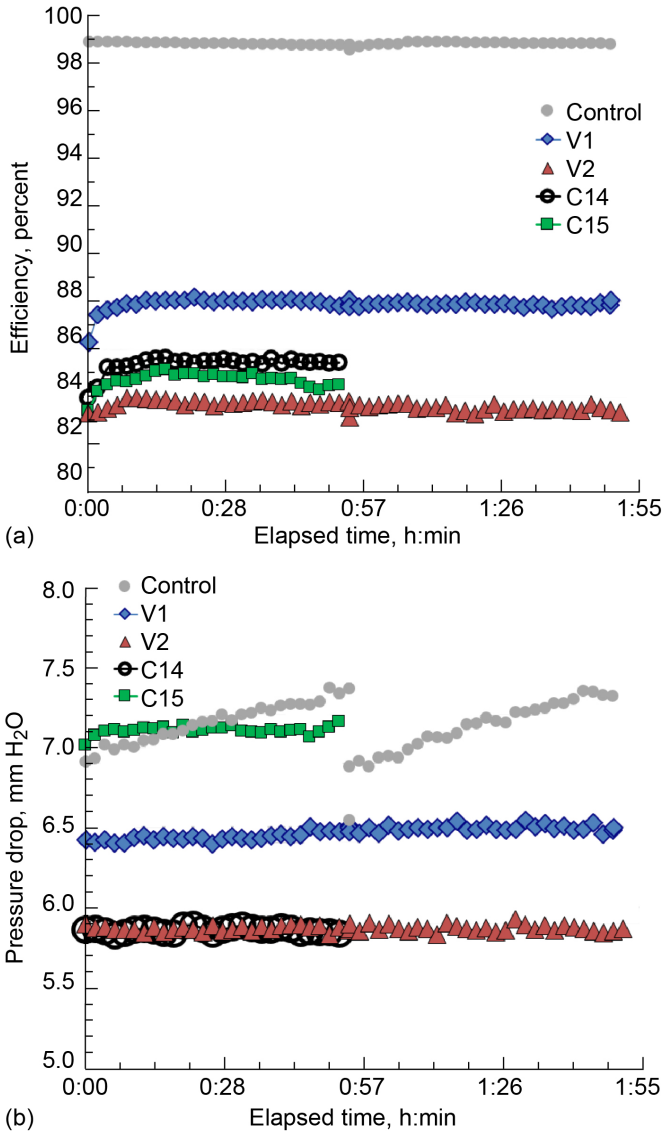

Figure 8.—Data from ~52- to 54-min loading tests conducted on polypropylene coupons, one control sample and four recharged samples. Some samples underwent two consecutive tests and corresponding data was stitched together in these plots. (a) Efficiency of 91-nm particle filtration. (b) Associated pressure drop.

3.2 Baselines for Discharged N95 Filter Media

Alcohol discharge yielded surface potentials of magnitude <0.5 kV and typical FE of ~35 percent. Potential measurements taken immediately after discharge were typically very close to zero, for example, –0.02 kV, but sometimes there were significant time delays prior to measurement. Larger values of discharged coupons are attributed to the unintentional pick up of transient charge from the environment, for example, triboelectric charges from handling or the plastic sample-container walls. Some representative alcohol discharged samples exhibited FE values of 37.3, 31. 3, and 36.0 percent.

A filtration test on a soapy-water-discharged coupon yielded a higher value of FE = 68.6 percent, which is comparable to 65.1 and 61.2 percent reported by others (Ref. 3).

3.3 Effect of Humidity on N95 Filter Media

The effect of humidity was investigated for one sample (UH10–B). As cut, it had a surface potential ranging from –0.13 to –0.15 kV as measured at 21.2 °C and 30 percent RH. After sitting in a humidified room (22.6 °C, 75 percent RH) for 8 h and remeasured in that condition, the surface potential appeared to be zero, ranging from –0.01 to +0.01 kV. This change is attributed to condensed (but visually undetectable) surface water having a screening effect. After subsequently allowing the sample to dry for about 65 h at 21 °C and 16 to 20 percent RH, the surface potential ranged from +0.16 to +0.21 kV. Filtration measurement then yielded 94.9 percent FE. Based on these results, it is postulated that the media was charged with a bipolar method by the manufacturer.

3.4 Charging Trials With Custom Corona Discharges

The descriptions and results of using corona discharge in attempts to recharge previously discharged N95 filter media are now presented in groups based on electrode configuration (see Figure 3). Since some shelved electrode configurations were tried again later, the attempts are presented in a sequence that is mostly, but not entirely, chronological. This semichronological presentation is used in order to show the evolution of and aid comparison of the experimental design factors (the electrode configuration, charging parameters, and procedural details). Changes to these configurations, parameters, and details are noted as they were introduced in the sequence. These trials and the corresponding results are summarized in Table I to Table IV.

The first configuration attempted for charging, Floating Coupon (FC), was very simplistic and the corresponding Trials are described in Table I. The LaB_6 emitter was connected with an alligator clip such that the high-voltage corona discharge of the LaB_6 crystal near the oven ceiling was directed down toward the floor of the oven. There, about 180 mm below, the sample was set in the center of a 150- by 150- by 1.5-mm PTFE sheet that provided electrical isolation from the metal floor of the oven. The sample slowly heated up and its temperature was periodically checked with the IR laser thermometer. After soaking for the allotted time at target temperature, the sample was removed with a nitrile-gloved hand and cooled with the fan at 8/8 speed. The Van de Graaff generator was on continuously during heat up and soak.

Filtration performance of coupons charged by this configuration was generally marginal (53.7 to 67.7 percent). The associated samples (A, B, D, and C from trials C1 to C4) were apparently not imparted with much charge, probably because they were rather far away from the emitter. Moreover, the limited convective airflow within the oven and the sample setter being made of insulating PTFE resulted in inconveniently long heat up times.

The next set of trials employed direct contact of the sample with a steel disk counter electrode. These are described in Table II. The first subgroup of these trials used the Floating Disk Stack (FDS) configuration in which the sample was positioned much closer to the corona discharge emitter by setting it on a stack of metal disks. The disk stack was electrically isolated from the metal walls, floor, and ceiling of the oven as shown in the far view and closeup pictures of Figure 9(a) and (b), respectively. In the previous configuration, the oven walls and floor were found to charge up and sometimes cause electrical shocks to the user. This phenomenon was redirected with the FDS configuration to concentrate such charging on the sample-setter surface. Another notable change was that an ionic dryer was used to direct high-velocity hot air into a port of the oven to help speed air-convective heating of the sample and disk stack. While this heating method also pushed negative air ions into the oven chamber, it is not thought to have been the primary mode of charging.

The first sample tried using the FDS configuration (UH9–4 from trial C5) exhibited only 59.0 percent FE. This may be due to its initial –2.9 kV surface potential measured immediately after recharging having decayed to at least –1.6 kV prior to being filtration tested the following day. Another contributing factor may have been the presence of unintended coronas from the LaB_6-emitter leads directed away from the sample.

TABLE I.—PRELIMINARY CHARGING TRIALS WHERE SAMPLE WAS CHARGED WITH LARGE DISTANCE TO EMITTER (d_{emit}) WITHOUT PURPOSEFUL COUNTER ELECTRODE USING FLOATING COUPON (FC) CONFIGURATION SHOWN IN FIGURE 3

Trial	Sample	Configuration	d_{emit}, cm	Temperature, °C	Time, min	Ionic-dryer oven heating	Sample surface potential, kV	Filtration efficiency, percent
C1	A	FC	17	120	3	No	No data	67.7 ± 0.3
C2	B	FC	17	120	3	No	No data	61.3 ± 0.4
C3	D	FC	17	120	2	No	–0.4	59.1 ± 0.5
C4	C	FC	17	120	1.3	No	No data	53.7 ± 0.2

TABLE II.—CHARGING TRIALS OF SAMPLES IN DIRECT CONTACT WITH METAL DISK COUNTER ELECTRODE ($d_{CE} = 0$)

[Trials involving multiple charging runs are noted. Reported values of sample surface potential and filtration efficiency were measured after final run. Configurations and distance to emitter (d_{emit}) are illustrated in Figure 3.]

Trial	Sample	Configuration[a]	d_{emit}, mm	Point source	Temperature, °C	Time, min	Sample surface potential, kV	Filtration efficiency, percent	Notes[b]
C5	UH9–4	FDS	20	LaB_6	120	3	–2.9→ –1.6	59.0 ± 1.45	Filtration tested day after charging.
C6	UH9–3	FDS	20	LaB_6	130	1	–2.5 to –3	80.9 ± 0.3	Dielectric sheathing added hereon. Stuck to petri dish container.
C7	UH5–2	GDMS	12.5	Al 7075	130	1	–2.5	85.4 ± 0.3	Two ionic dryers.
C8	UH56–3	GDMS	12.5	Al 7075	130	1	–2.5	85.5 ± 2.4	Two ionic dryers. Loud hissing.
C9	UH9–2	FDMS	25	LaB_6	130	1	–3.3 to –2.9	75.9 ± 0.2	Two ionic dryers. LaB_6 emitter. Waited 4 days to measure.
C10	UH9–4	FDMS	6.5	LaB_6	140	1	–3 to –2.5	81.3 ± 0.2	Six runs. Waited a week to measure.
C11	UH56–4	FDS	6.5	LaB_6	145	0.5	–3.2 on single ply	80.4 ± 0.2	PRS. SERM.
C12	UH56–5	FDS	6.5	LaB_6	145	0.5	Not measured	79.1 ± 0.2	PRS. SERM.
C13	UH56–6	FDS	6.5	LaB_6	145	1	Not measured	81.9 ± 0.2	PRS. SERM.
C17	UH6–1	IFD	13	LaB_6	120	0.5	–2.6	75.0 ± 0.1	Waved to cool at room temperature. Strong movement.
C18	AB1	IFD	8.5	LaB_6	60	0.67	–2.4 to –1.7	83.2 ± 0.3	Moderate movement.
C19	UH5–2	IFD	4.5	LaB_6	80, 100	0.5, 0.5	–2 (each ply)	85.4 ± 0.1	PRS at different times. SERM.

[a]Floating Disk Stack (FDS). Floating Disk-Magnet Stack (FDMS). Grounded Disk-Magnet Stack (GDMS). Individual Floating Disk (IFD).

[b]Plies recharged separately (PRS). Strong electrostatic repulsive movement (SERM).

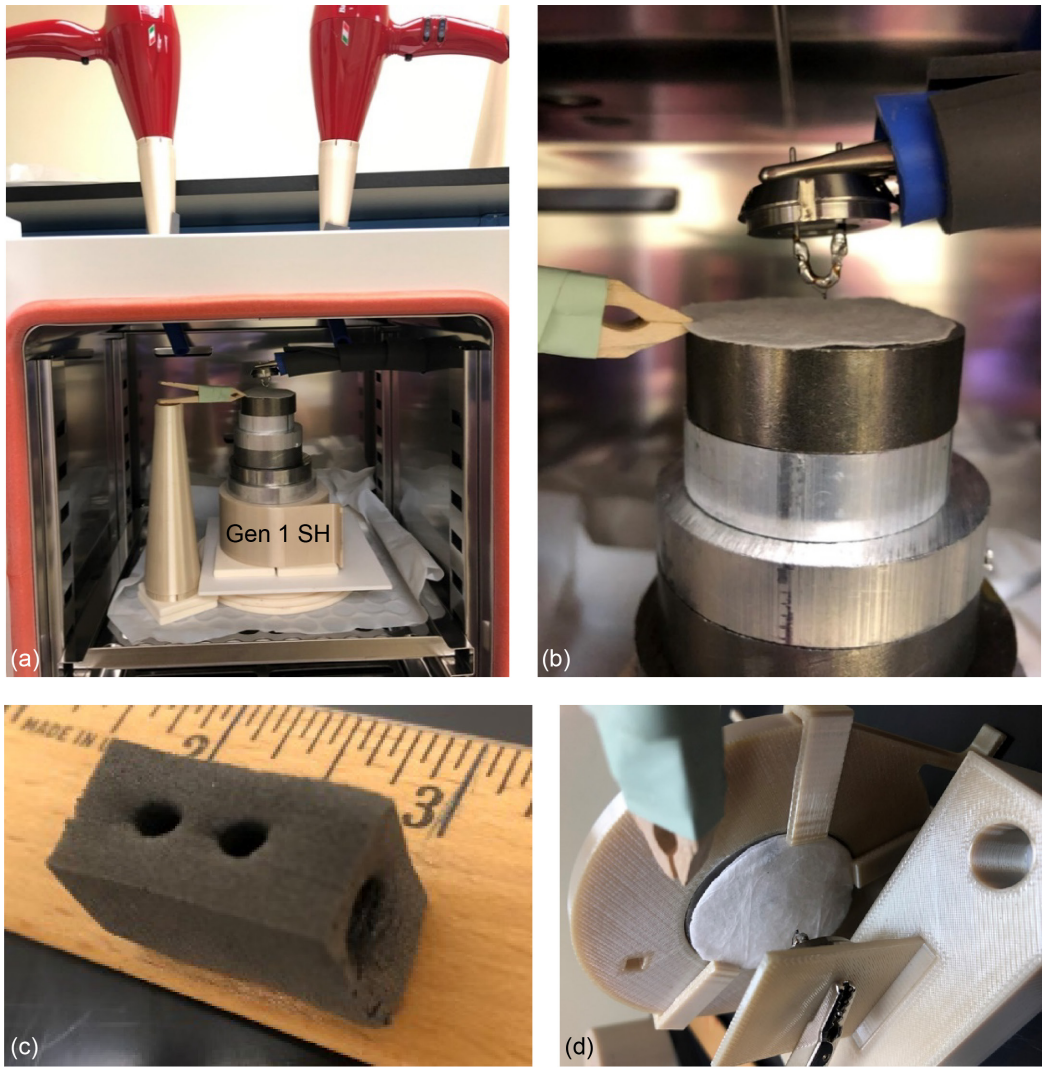

Figure 9.—Equipment and setups of electrically similar Floating Disk Stack (FDS) and Individual Floating Disk (IFD) configurations of charging. (a) FDS setup using electrically isolated metal-disk stack along with electrically insulating clothespin for sample removal. Sample holder (SH). (b) Closeup view of LaB_6 emitter pointing at 51-mm-diameter filter coupon resting on top of disk stack and being gripped by clothespin whose metal spring is wrapped with high-temperature tape. (c) Dielectric shield fashioned out of nylon foam for emitter-attaching alligator clip. (d) IFD setup where the emitter was held in the emitter holder, a single steel disk in the electrode holder replaced the disk stack, and the sample was held in position by slight overlap of clips onto the electrode perimeter and was removed from above with the clip.

These undesired corona discharges were subsequently passivated by placement of dielectric screening covers. Covers were fashioned from nylon foam for the alligator clip (see Figure 9(c)) and ~3-mm cubes of silicone cut from tubing for the LaB_6-emitter leads (not shown) and applied during charging trials of the next sample, UH9–3. This sample tested at 80.9 percent FE after trial C6. The higher result is attributed to such dielectric passivation and the facts that this sample (1) was charged at slightly higher temperature and (2) ultimately underwent six charging runs of 60 seconds each. After the final charging run, it exhibited potentials of –3 and –2.5 kV on respective sides and had such strong movement that it clung to the lid of the plastic petri dish container.

During charging of the next two samples (UH5–2 and UH56–3 in trials C7 and C8), other changes may have contributed to slightly improved performance (85.4 and 85.5 percent FE, respectively). The disk stack was grounded via an attached wire and the 51-mm NdFeB magnet was attached to the top of the stack to try to increase the charging current as it has been found that a negative corona current may be increased via an applied magnetic field (Ref. 80). These constituted the Grounded Disk-Magnet Stack (GDMS), which except for the changes noted appeared

similar to the previously used FDS setup. The new GDMS setup matched Figure 9(a) to (c) except for the changes noted previously. Also, the emitter distance was reduced to 12.5 mm and the Al 7075 emitter was used instead of the LaB_6 crystal. It was speculated that deleterious oxidation could occur on the LaB_6 surface whereas the surface oxide of Al provides good passivation. Moreover, a second ionic dryer using the same settings was added to the setup for faster heating. Prior to beginning heating with the ionic dryers, the corona hissing noise was notable and unusually loud, and parasitic coronas were looked for but not detected.

For the next sample (UH9–2 of trial C9), a few changes were made to the setup and procedure. First, the disk stack was disconnected from ground. This produced the Floating Disk-Magnet Stack (FDMS) configuration of Figure 3. Also, the emitter was changed back to the LaB_6 and the emitter distance was increased to 25 mm. After three charging attempts, the sample movement was strong, and surface potential ranged between –3.3 to –2.9 kV immediately after the final attempt. However, this sample was deprioritized in the filtration-measurement queue due to it exhibiting reduced movement the next day. When it was finally filtration tested 4 days after charging, the result was 75.9 percent FE.

In the next trial (C10 with sample UH9–4), temperature was raised to 140 °C, the setup remained FDMS, and the emitter distance was ultimately lowered to 6.5 mm over the course of six charging attempts. Initial examination of the sample indicated strong charge and movement of the sample, but this decayed significantly overnight before eventual measurement that indicated 81.3 percent FE.

For the next set of samples (UH56–4, UH56–5, and UH56–6 of trials C11 to C13), the configuration was reverted to the FDS as the magnet was removed. Also, the temperature was increased to 145 °C and the two different plies of the samples were charged separately. The latter two samples were not measured with the static meter in an attempt to preserve imparted charge, and the last sample was charged for a significantly longer time. All three of these samples exhibited strong movement and self-repulsion within dual-ply samples. Yet, all of these samples had FE of about 80 percent and varied by a few percent at most between them.

Charging at lower temperatures was later revisited and further explored using the Individual Floating Disk (IFD) configuration. The IFD configuration is very similar to the FDS configuration from an electrostatic standpoint and employs a single 51-mm metal disk rather than a stack of metal disks. In the IFD setup, the sample was held against the metal disk within the electrode holder using clips (as shown in Figure 9(d)) and was removed after charging with the clothespin or an Ultem® clip.

Three samples charged with the IFD setup ultimately progressed to filtration test. For the first sample (UH6–1 of trial C17), the 120 °C temperature was used for 30 seconds rather than the much longer time tried earlier with sample UH9–4 at the same temperature (3 min). Before these IFD experiments, it was considered that perhaps somehow the longer duration previously used was detrimental because the reference of contemporary focus (Ref. 22) used a much shorter duration of 10 seconds. One other difference for UH6–1 was that the coupon was cooled by waving in the air at room temperature in order to avoid any potentially neutralizing effect of fan-blown air. However, these changes only resulted in a marginal improvement up to 75 percent FE.

IFD-based recharging of the second and third samples of this set (AB1 and UH5–2 of trials C18 and C19) was done at significantly lower temperatures. The former sample was charged at 60 °C, and the latter had its plies recharged separately at 80 and 100 °C, respectively. The higher temperature for the second ply was used because it did not seem to charge as well as the first ply at the 80 °C temperature. After such treatments, both samples seemed to be well charged, and the subsequently measured FE was higher by roughly 10 percentage points. Temperatures lower than 60 °C were not explored based on (1) the notion of the charge needing to be "frozen in" and (2) the literature known at the time, which suggested that higher and more stable surface potentials could be achieved from charging at elevated temperatures (Refs. 22 and 26).

Notwithstanding that 145 °C was perhaps too hot for the treatment of an actual N95 mask, the FE values from the ungrounded FDS configuration fell well short of the goal. Yet, it was noted that the GDMS setup appeared to result in slightly higher FE values at more reasonable temperature. From this, it was speculated that current flux through the sample to ground was the more important advantageous factor rather than the use of the magnet. It was also assessed that there should be no physical contact between the sample and a hot grounded metal disk that offered a path for discharge from the sample.

Therefore, the configuration was changed and Through Current (TC) charging attempts were made with a nonzero distance between the sample and ground electrode. Besides the adoption of the TC configuration, another notable procedural change was that the electric field was maintained while these samples were cooled with forced air after charging at the target temperature. These experiments are described in Table III.

The first subgroup of these attempts comprised trials C14 to C16 for which the sample was cooled into the 50 to 60 °C range while in the oven and then removed for further fan cooling to ~25 °C. The TC schematic in Figure 3 was first physically

TABLE III.—CHARGING TRIALS USING THROUGH CURRENT (TC) CONFIGURATION

[Sample surface potential from final charging run of trial is provided. Notes describe controlled values of point source voltage and whether trial was done in oven or temperature-controlled box in which cooling was always done with fan at full power. Configurations, distance to electrically grounded counter electrode (d_{CE}), and distance to emitter (d_{emit}) are illustrated in Figure 3.]

Trial	Sample	Point source (PS)	d_{emit}, mm	d_{CE}, mm	Temperature, °C	Time, min	Sample surface potential,[a] kV	Filtration efficiency, percent	Notes
C14	AB1	LaB_6	8.5	4	120	1	–2.6 to –2.9	85.1 ± 0.4	Oven, compressed air
C15	BC1	LaB_6	10	14	108	1.5	–2.1 to –2.2	82.7 ± 0.1	Oven, compressed air. 100 °C/2 min pretrial.
C16	BC3	LaB_6	12	15.5	140	1	–2.5	85.8 ± 0.4	Oven, fan cool, and compressed air. Pretrial: 120 °C/1 min.
C22	UH6–1	Steel needle (SN)	27	1.5	80	0.5	SEM	88.6 ± 0.3	Box. PS at –16 kV.
C23	AV32–1	SN	27	1.5	85	0.5	SEM	85.4 ± 0.1	Box. PS at –16 kV.
C24	AV31–1	SN	27	1.5	77.5	0.5	–2.4 to –2.7, SEM	84.5 ± 0.6	Box. PS at –17 kV. Two pinholes fixed with glue.
C25	AV32–1	SN	28	1.5	120	1	–2.3 to –2.0, SEM	85.6 ± 0.3	Box. PS at –15.5 kV. Pretrials: Ionic dryer → no charge. At 145 °C in box yielded –1.5 kV.
C26	AV31–3	SN	28	1.5	75	5	VSEM. Defied gravity in dish.	85.9 ± 1.1	Box. PS at –16 kV. Pretrial at 62 °C/2 min yielded –1.4 kV.
C27	AV31–4	SN	28	1.5	120 to 121	6	SEM	84.4 ± 2.2	Box. PS at –15.5 to –16 kV. Arced to produce hole with 1 min remaining. Hole fixed with glue.

[a]Strong electrostatic movement (SEM). Very strong electrostatic movement (VSEM).

manifested with a setup employing an improvised emitter holder shown in the closeup photograph of Figure 10(a), which was used for charging samples AB1 and BC1 of trials C14 and C15. A far view is shown in Figure 10(b) in which white and off-white PTFE and alumina parts can be seen—these were used for their good electrical insulation properties. An attempt at maintaining axial alignment was made with the Gen 1 track highlighted in Figure 10(c) and apparent in Figure 10(a) and (b). A more advanced manifestation of the TC configuration is shown in Figure 11(a), which was moved inside the oven for charging of sample BC3 in trial C16. The 3D-printed emitter holder of this setup includes a built-in alignment track and is highlighted in Figure 11(b) along with accompanying accessories such as insert cards for fixed and aligned positioning of corona point sources and hose holders for directing heating and cooling airflows onto the sample.

Samples of all three trials (C14 to C16) exhibited FE in a relatively narrow ~3-percent range (i.e., 82.7 to 85.8 percent) despite considerable variations in charging temperature, time, and electrode positioning. It seems plausible that variability of Van de Graaff generator voltage output (Ref. 69) might have influenced these and all aforementioned C-series results. Two of these samples also underwent 52 min of loading testing. The results are plotted in Figure 8, where it can be seen that FE values are close to the instantaneous results and were retained throughout. A lower proportion of particles being captured compared to the control sample might be associated with the greater stability and smaller slope of the C14 and C15 pressure-drop data that implied no clogging.

Similar charging of other coupons was attempted with additional use of the hose holders as shown in Figure 12(a) (far view) and Figure 12(b) (closeup view). However, these trials resulted in samples with partial melting due to nonuniform heating at close distance or others that did not seem worthy of filtration test. The latter involved cooling with a directed flow of cold nitrogen gas from the pressure release of a liquid-nitrogen

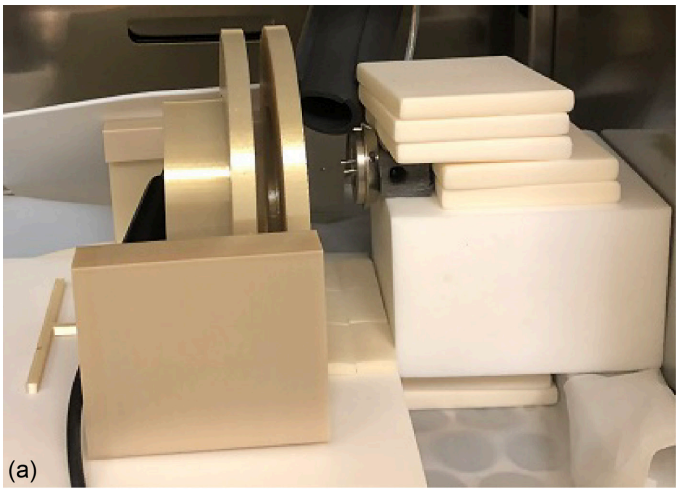

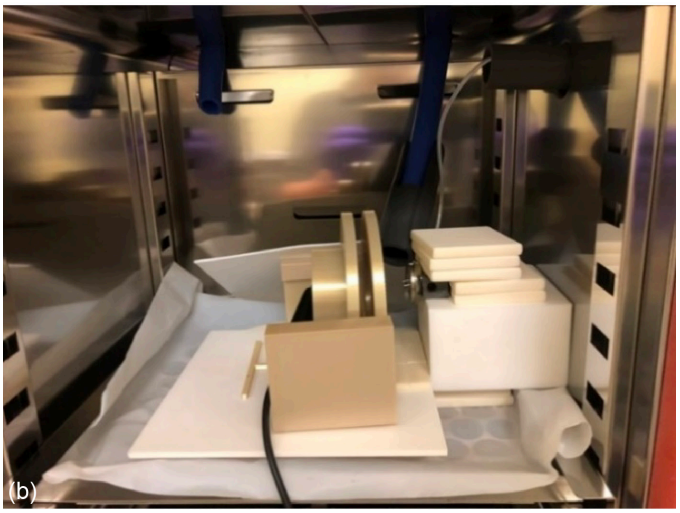

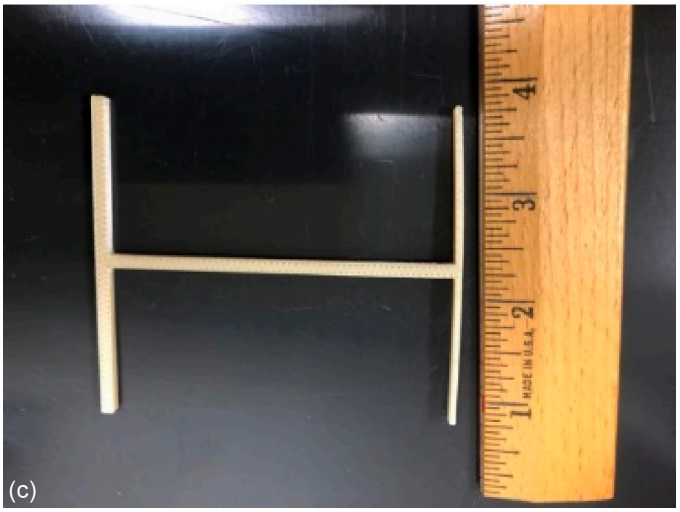

Figure 10.—Laboratory setup and key part thereof. (a) Closeup view of the earlier laboratory setup of the Through Current (TC) configuration with improvised emitter holder and hot-air line directed at sample. Includes dielectric cover for emitter-attaching aligator clip. (b) Far view. (c) Gen 1 alignment track.

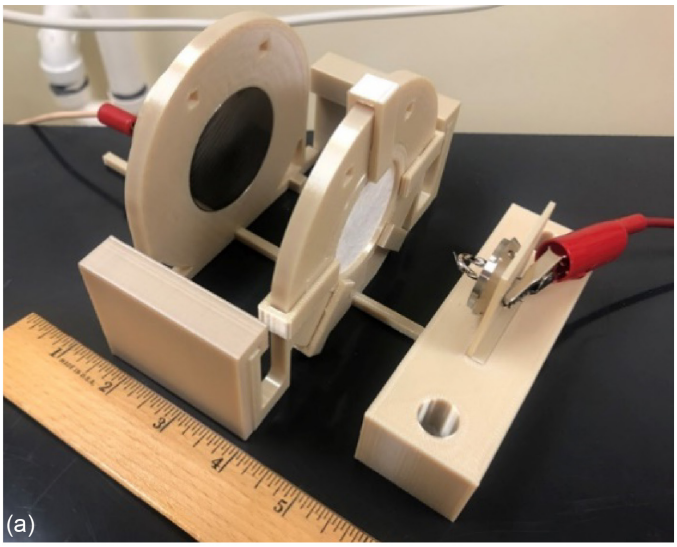

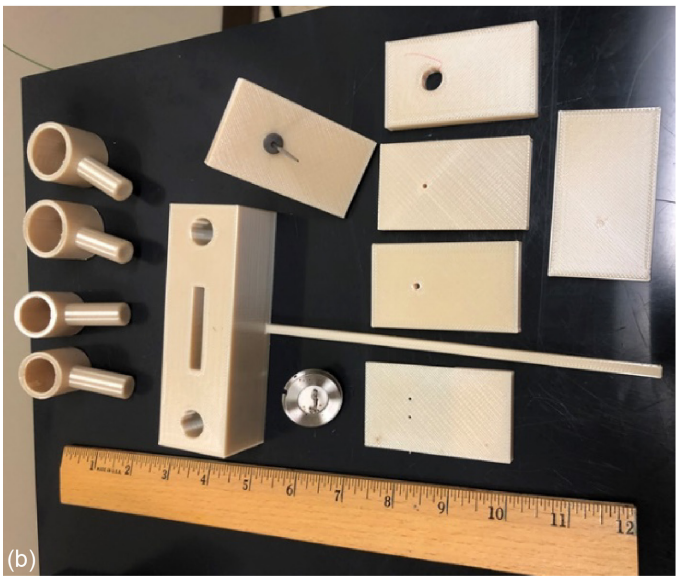

Figure 11.—Three-dimensional printed emitter-holder setup and components. (a) Setup corresponding to the Through Current (TC) configuration, loaded and clipped Gen 4 sample holder, loaded Gen 2 electrode holder connected to electrical ground, and LaB_6-loaded emitter holder. (b) Emitter holder including built-in alignment track and associated accessories such as air-hose holders, LaB_6 emitter, and insert-card emitter adapters including one with loaded needle through nylon-foam cushion.

dewar while the electric field was maintained. The intent was to improve “freezing in” of trapped charge via more rapid cooling. However, this treatment seemed to promote arcing during cooling as well as a lack of electrostatic movement for the processed coupons. Cooling with compressed air was also excessively time consuming due to oven thermal mass and instances when samples came loose from the sample holder due to forceful cooling-air windage. Therefore, trials in the oven were ceased.

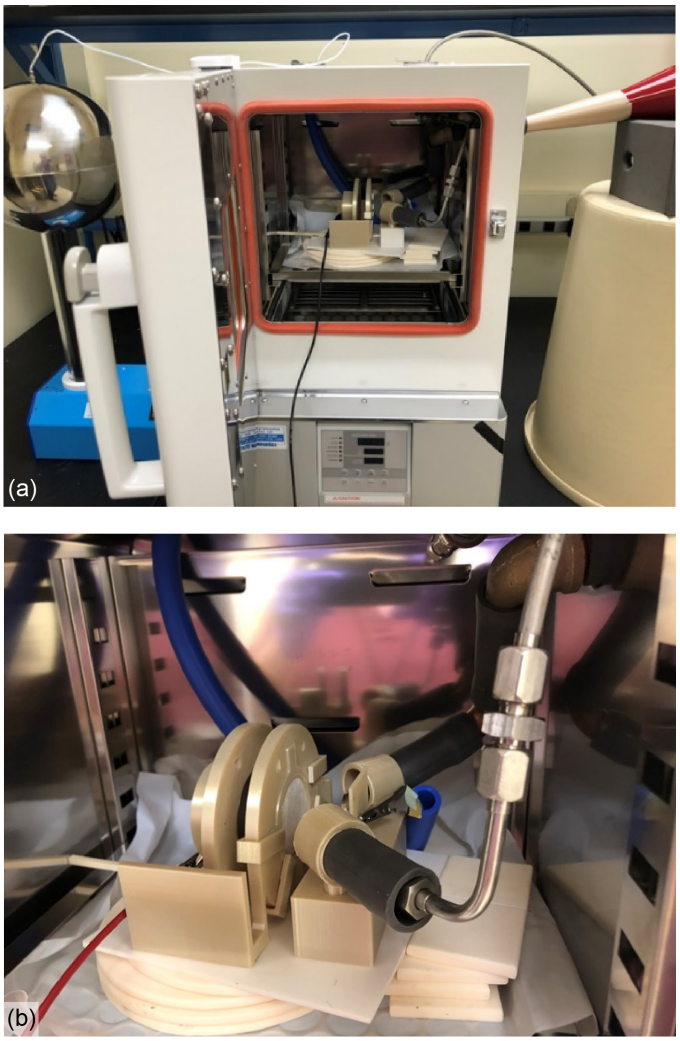

Figure 12.—Through-filter corona charging approach executed in oven showing (a) Van de Graaff generator (left) and ionic-dryer (right) inputs and (b) how heating and cooling flows were directed at sample via hose holders.

Additional TC-based charging attempts were conducted inside a manually constructed temperature cell, which was essentially a box constructed of 13-mm-thick nylon foam and high-temperature glue. The thermal mass of this cell and its contents was much smaller than that of the oven and this greatly reduced the heating and cooling times of the charging experiments. During most of the trials using the temperature cell, the ground-to-emitter voltage was well controlled and is noted (Table III). For all described tests, temperature control of the cell was accomplished using hot air from the programmable Poniie heat gun, which was funneled into the cell via plumbed silicone tube. The gun setting was higher during heat up and then lowered and varied as needed in order to achieve stability at the target temperature. The hot air was directed onto the PPSF heat shield to avoid sample melting, and the sample was heated indirectly via convective airflow inside the cell. The ionic dryer was considered for heating during early experimentation, but it was decided that its additional ion flux would add an additional level of complication to the experiment. During heat up and charging at target temperature, the box lid was kept closed (Figure 13(a)). Sample cooling was performed by removing the box lid and directing the fan at max power towards the loaded bottom of the box (e.g., Figure 13(b) and (c)) as the electric field was maintained. This cooling method was effective at rapidly cooling the entire temperature cell while not disrupting the electric field experienced by the sample since its positioning and that of the electrode configuration were unaffected by such windage. All electrode configurations employed a current through the sample. The ground electrode steel disk was held with the electrode holder (Figure 13(b) and (c)) except in cases where it was gripped into the backside recess of the sample holder with wide-jawed clips, which corresponds to d_{CE} = 1.5 mm and is shown in Figure 14. In some cases, which are noted, the sample was contacted with a metal screen using configurations defined by Figure 3. Photographs corresponding to TCES and TCGS configurations are shown in Figure 15(a) and (b), respectively. A K-type thermocouple with alumina sheathing was used to measure temperature and was positioned behind the ground electrode to avoid disrupting the electric field distribution experienced by the sample. Once the temperature reached ~25 °C during cooling, the electric field was switched off and the sample was removed for evaluation.

The first six charging trials taking place in the temperature cell (C22 to C27) were all performed with approximately the same voltage and using the counter-electrode setup shown in Figure 14. Namely, the voltage was at or near –16 kV, the sample holder was pushed all the way back in the box from the emitter (d_{emit} = 27 to 28 mm), and the ground electrode was fixed to the back of the sample holder (d_{CE} = 1.5 mm). This geometry is thought to have presented a relatively uniform electric field to the sample since it was far from the emitter point source and close to the disk electrode. The first three trials explored the reproducibility and temperature sensitivity pertaining to an ~80 °C charging temperature using a constant and relatively short ~30-s charging time. The latter three trials explored the use of a higher temperature (120 °C) and longer charging times of 5 to 6 min. Despite such significant variation of parameters, the different conditions all resulted in charged samples exhibiting strong electrostatic movement and good filtration behavior in a relatively narrow range of performance, 84.2 to 88.6 percent FE. As noted for some of the trials, similar pretrials conducted at 62 and 145 °C produced results that were deemed unworthy of filtration testing. A similar trial at 100 to 105 °C, which is not listed in the tables, yielded a similar result. For trial C27, the charging condition appeared stable until

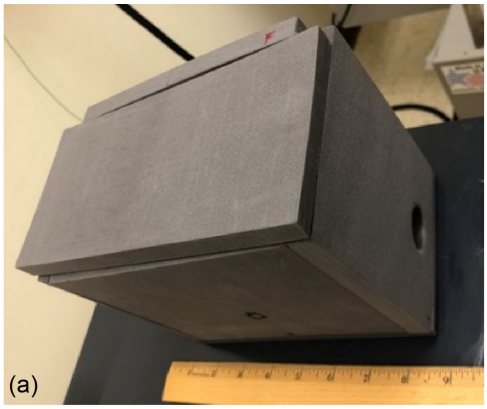

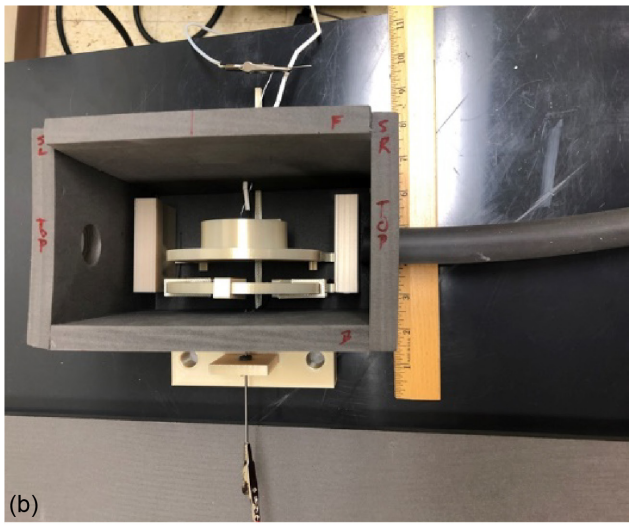

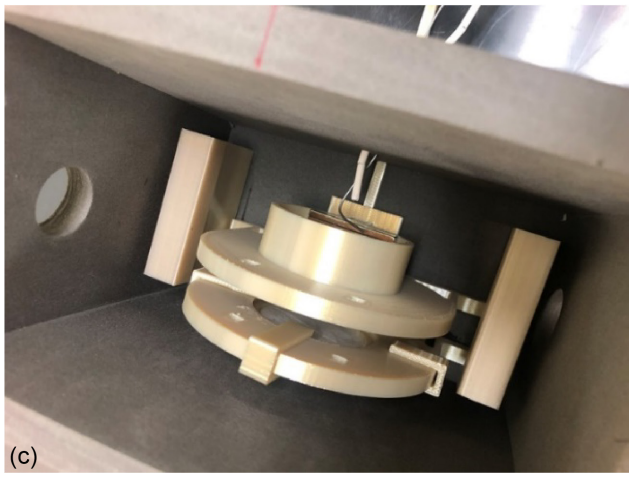

Figure 13.—Temperature control cell. (a) With lid on and without any inputs. (b) Configured for corona charging by being loaded with electrode and heat-shielded sample holders, as well as plumbed with steel-needle emitter, alignment track, grounding lead, thermocouple, and hot-air hose (c) Closeup view of (b).

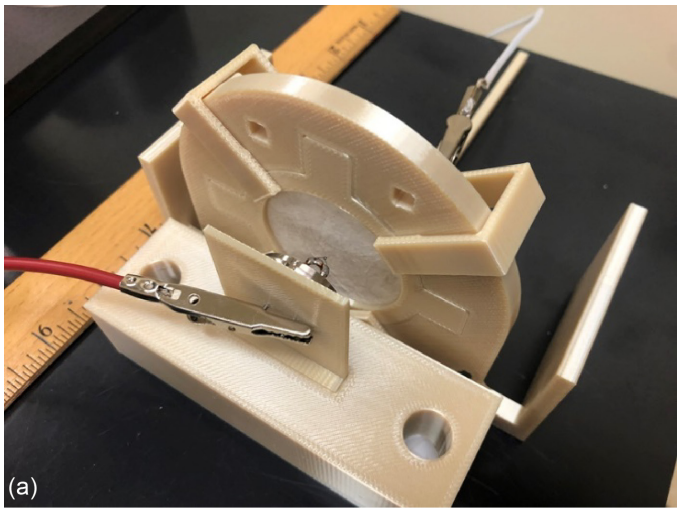

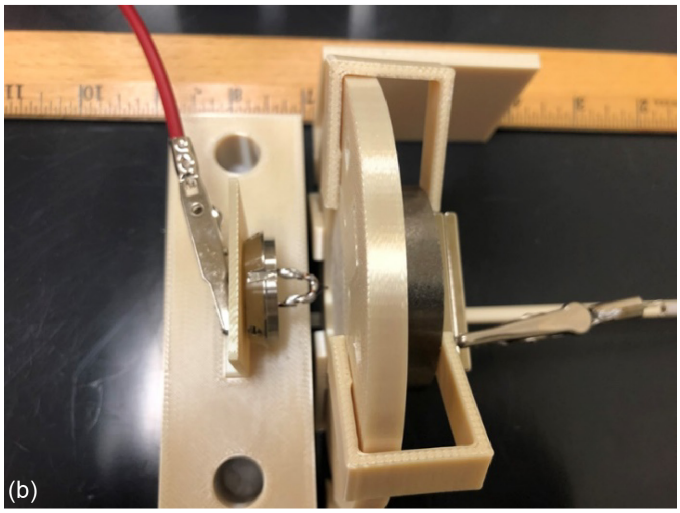

Figure 14.—Laboratory manifestation of Through Current (TC) configuration in which distance between sample back plane and electrically grounded counter electrode (d_{CE}) is 1.5 mm because steel-disk electrode is affixed directly to sample holder via wide-jawed clips. (a) Front view. (b) Side view.

a single event of arcing to ground occurred prior to the final minute of the 5 min. This was thought to indicate a detrimental loss of sample electrical potential and subsequently motivated shorter hold times. The small hole produced in the sample was filled with glue prior to filtration test.

During the next set of trials in the temperature cell, metal screens were placed against the sample because during informal experimentation, it was observed that screens had strong interactions with coronas from the Van de Graaff generator. However, before describing those, the first trials of charging with screens are discussed (i.e., trials C20 and C21). These are described in Table IV and occurred inside the oven while using

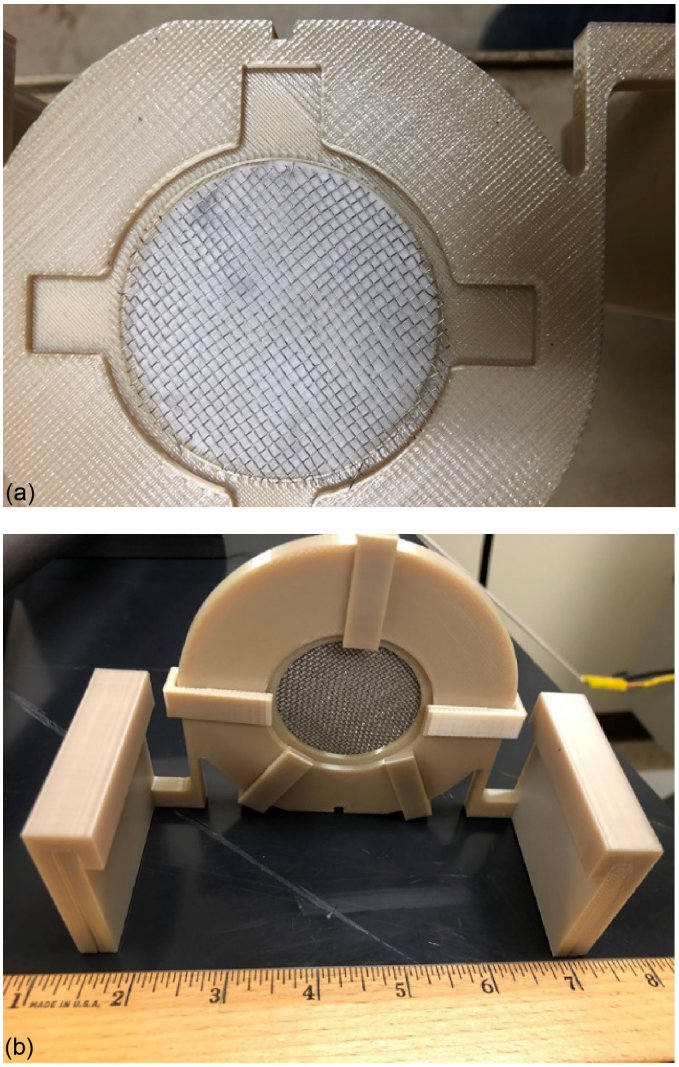

Figure 15.—Positioning of metal screens with filter coupon. (a) Thin screen in front of filter coupon as used for configuration Through Current with Emitter-Side Screen (TCES) before attachment of retainer ring. (b) Stiff screen behind filter coupon as used for configuration Through Current with Ground-Side Screen (TCGS) in backside view of loaded Gen 4 sample holder.

the Van de Graaff generator with samples UH6–11 and UH9–2, respectively. For the former, the screen was electrically floating and was positioned in contact with and behind the sample in the sample holder in a FS setup. After charging, the sample exhibited very strong electrostatic movement. For the latter sample, a pretrial was first conducted using a TCES setup with nominal trial parameters, and this resulted in a –2.5 to –2.7 kV potential. Then, the sample was placed between and in direct contact with two screens within the sample holder in a TCEGS setup for an attempted recharge. Despite this resulting in minimal electrostatic movement, the sample was filtration tested anyway and actually exhibited slightly higher FE than UH6–11 at 85.1 versus 82.6 percent FE.

An additional group of trials (C28 to C31), which further explored the effect of screen usage in the temperature cell, are also described in Table IV. These tests effectively probed the reproducibility around ~80 °C target temperature and sensitivity to other parameters in pursuit of the best-of-technique result in trial C22, which is close to the 75 °C temperature that was used in one study (Ref. 22) to obtain improved charging compared to 21 °C. In this group of trials, the voltage was also changed to –20 kV, and the electrode holder was reintroduced such that d_{CE} increased from 1.5 mm during trials C22 to C27 up to 6.6 mm. These changes were expected to increase the magnitude of electric potential at the sample position since the ground-to-emitter voltage magnitude increased 25 percent, and the sample position was shifted from 5 to 19 percent of the ground-to-emitter distance. Using Kirchhoff's voltage law and a simplifying assumption of a linear rise in voltage magnitude across the ground-to-emitter distance, the electric potential magnitude at the sample position can be estimated to be ~4.2 to 4.8 times greater for this group of trials.

For this group, trial C30 provided a no-screen baseline for comparison. Trials C28 and C29 employed the thin screen in contact with the sample on the emitter and ground side. This corresponded to configurations TCES and TCGS, respectively. For these two trials, corona noise was audible and for the former sample (AV32–1), nonarcing discharges from the screen to ground were observed. The sample was charged for 5 min, filtration tested, and subsequently was recharged without being alcohol discharged first in trial C31 for an additional 1.5 min. In this later trial, the screen was of the thicker type and contacted the sample on the ground rather than the emitter side. As can be seen in Table IV, the FEs measured from this group of trials were very similar despite the variations to the experimental conditions.

TABLE IV.—TRIALS EXPLORING THE USE OF METAL SCREENS

[All trials used needle point source (PS) unless otherwise noted for LaB_6 emitter. Screen type and controlled voltage of PS are noted when applicable. Configurations, distance to electrically grounded counter electrode (d_{CE}), and distance to emitter (d_{emit}) are illustrated in Figure 3.]

Trial	Sample	Configuration[a]	d_{emit}, mm	d_{CE}, mm	Temperature, °C	Time, min	Sample surface potential,[b] kV	Filtration efficiency, percent	Notes[b]
C20	UH6–11	FS	11.5	0	80	0.33	Not measured	82.6 ± 0.3	VSEM, thin screen. LaB_6.
C21	UH9–2	TCEGS	5	13	80	0.33	Not measured	85.1± 0.3	LaB_6. Minimal electrostatic movement, thin screens.
C28	AV32–1	TCES	28	6.5	81	5	SEM	87.4 ± 0.3	PS at –20 kV, thin screen. Corona noise, nonarcing discharges to ground.
C29	J	TCGS	28	6.5	80	2	SEM	86.4 ± 0.2	PS at –20 kV, thin screen. Corona noise, no arcing, no observations of discharges.
C30	UH6–1	TC	28	6.5	80	2	SEM	85.7 ± 0.4	PS at –20 kV.
C31	AV32–1	TCGS	28	6.5	80 to 81	1.5	SEM	86.5 ± 0.2	Sample not discharged after previous recharge. Thick screen. PS at –20 kV.
C32	SW1	TCGS	28	6.5	99 to 102	5	–3.0, VSEM	76.2 ± 0.9	PS at –20 kV. Pretrial 80 °C/5 min → –1.6 kV. Two days rest before filter test.
C33	AV32–3	TC	22.5	12	80 to 82	3	MEM	80.0 ± 0.2	PS at –20 kV.
C34	LD1	TCGS	4	30.5	80	3	MEM	74.2 ± 2.5	LaB_6.

[a]Floating Screen (FS). Through current (TC). Through Current With Emitter-Side Screen (TCES). Through Current With Ground-Side Screen (TCGS). Through Current With Emitter- and Ground-Side Screens (TCEGS).

[b]Point source (PS). Strong electrostatic movement (SEM). Very strong electrostatic movement (VSEM). Moderate electrostatic movement (MEM).

That trial group motivated an additional three runs (C32 to C34, Table IV) with parameter alterations that were not successful in improving FE performance. The first run (C32) used a ~100 °C/5 min condition while the spacings were kept the same and a thick screen was deployed behind a soap-and-water discharged sample in configuration TCGS. This was done after an 80 °C/5 min pretrial yielded modest electrostatic movement and –1.6 kV potential. The ~100 °C temperature was intriguing because it had not yet been tested in the temperature cell. Despite exhibiting extremely strong electrostatic movement and a potential of –3.0 kV immediately after charging, the resulting sample had 76.2 percent FE when tested 2 days later. For the second run (C33), the screen was removed but the sample was shifted several millimeters closer to the emitter (i.e., to 35 percent of the ground-to-emitter distance, which itself was kept constant). Using the simplified calculation described previously, the electric potential of the sample was expected to be higher by a factor of 1.8 compared to the previous trial group. However, the resulting FE was 80 percent. For the third run (C34), the stiff screen was used again in the TCGS configuration, and the aforementioned approach to increasing sample surface potential was further extended. Namely, the –325 kV (nominal) Van de Graaff generator was used without voltage control, and the sample was positioned 4 mm away from the emitter. This position corresponded to 88 percent of the ground-to-emitter distance and a simplified predicted potential ~75 times greater than that for the previous trial group. However, 74.2 percent was the resulting FE, perhaps due to a loss of electric-field uniformity across the sample.

Because electric potential measurements of full masks were found to be significantly influenced by nonactive components, recharging attempts on full N95 masks were very limited. In one trial, a mask that had its charge erased with alcohol was affixed to the Van de Graaff generator and wanded with its manufacturer-provided spherical counter electrode (at electrical ground) for a few minutes amid loud corona discharge hissing. This process was very similar to that described in Reference 68 except for the opposite polarity of the employed generator. The result was a mask with a large-magnitude negative electric potential. However, this potential was measured to have dissipated after breathing through the mask for 1 min. Therefore, filtration testing was not done.

3.5 Trials With Ionic Hair Dryer

Charging attempts with the ionic hair dryer were made using the configurational variants defined in Figure 5. Some aspects of the laboratory setups employed are shown in Figure 16. Table V shows the corresponding results of 15 trials that ultimately led to a filtration measurement. The values given refer to the final charging run conducted within each trial. In several trials, charging “dry runs” were executed because the

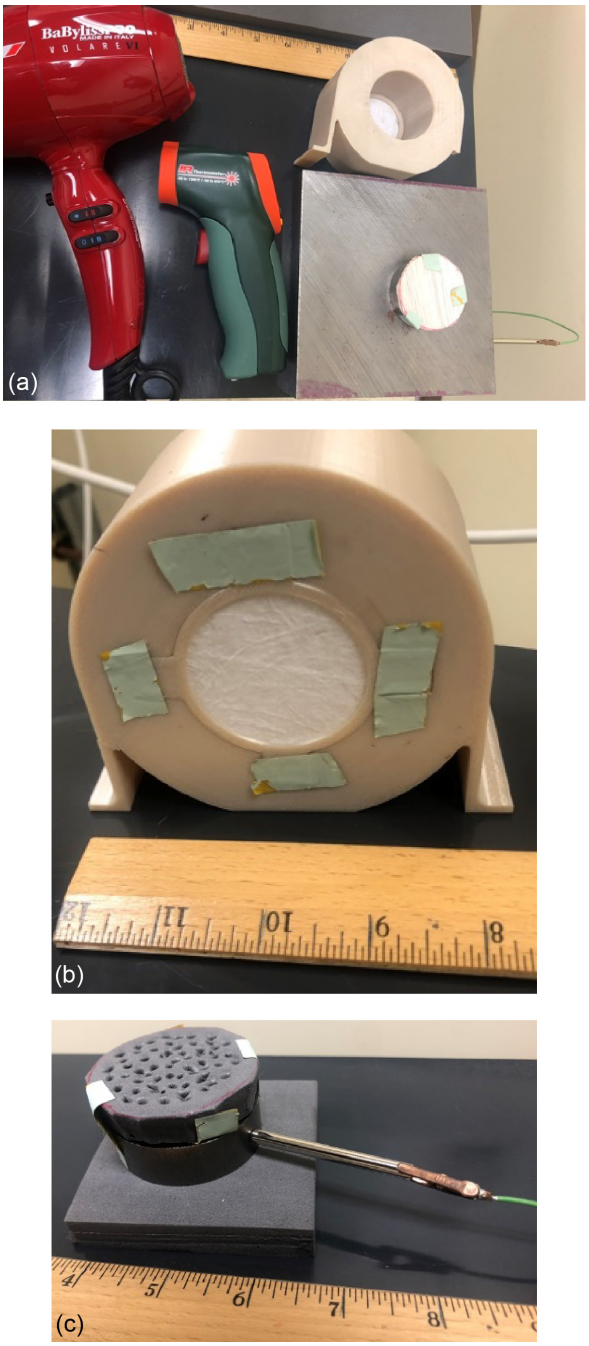

Figure 16.—Equipment and materials used for ionic-dryer method charging attempts. (a) Ionic hair dryer, infrared (IR) laser thermometer, and pedestal composed of balsa-wood disk attached on top of metal disk via high-temperature tape with steel plate underneath to provide connection to electrical ground via wire clipped onto magnet. (b) Gen 1 sample holder with filter coupon affixed via retainer ring and high-temperature tape. In Ionic-Dryer Arrangements 2, 3, and 4 (see Figure 5), this was placed coupon-side down on top of pedestal. (c) Alternate pedestal associated only with Ionic-Dryer Arrangement 4. Here, grounding disk rests on nylon foam and lies beneath an affixed barrier disk made of nylon foam with through holes.

coupon was subsequently assessed after each to have insufficient charge prior to the final run that apparently produced a well-charged coupon worthy of filtration testing.

As can be seen, the ionic-dryer method was able to achieve a relatively good performance (82 to 91 percent FE) for nearly half of these trials. Such capability is primarily attributed to the strong aerodynamic force and large flux of negative ions provided by the specific ionic-dryer unit. Yet, no combination of parameters met the goal of 95 percent FE. Also, good reproducibility of surface potential and coupon movement after a given charging process was not established. One or more lurking variables are thought to explain this. For example, one such variable could be the air pressure on the coupon as determined by imperfect aim of the ionic dryer and air leakage around the ground electrode at the downstream end of the sample-holder borehole in Ionic-Dryer Arrangements 2, 3, and 4.

TABLE V.—CHARGING TRIALS USING IONIC DRYER IN DIFFERENT ARRANGEMENTS SHOWN IN FIGURE 5

[Distance in holder (d_{in}) > 0 for nozzle insertion and d_{in} < 0 for standoff.]

Trial	Sample	Arrangement	Temperature, °C	Time	Sample surface potential,[a] kV	Filtration efficiency, percent	Notes and deviations from standard process[a]
V1	UH11–C	A	120	20 s	–2	89.1 ± 1.4	Charged one ply at a time. Potential measured on one ply only prior to first filtration test. Loading test followed.
V2	UH11–D	A	120	20 s	–1.2	84.9 ± 0.3	Charged one ply at a time. Low-velocity setting. Subsequently loading tested.
V3	UH10–C	B	105	30 s	–2.0 to –2.2	60.2 ± 1.4	d_{in} = 5 mm. SEM.
V4	UH11–B	B	105	1 min	Not measured	66.1 ± 0.8	d_{in} = 5 mm. Some movement.
V5	UH10–B	B	105	2 min	–0.6	83.4 ± 0.4	d_{in} = 5 mm. Dry run (120 s) resulted in –0.9 kV.
V6	UH10–D	B	105	20 s	Not measured	59.6 ± 0.6	d_{in} = 15 mm. Low-velocity setting. Cool at 8/8 fan speed for 15 to 20 s. SEM.
V7	UH10–A	B	105	5 min	Not measured	82.3 ± 0.5	d_{in} = 5 mm. Good movement.
V8	UH9–3	C	100 → 110	20 s	–0.6 to –0.95	67.1 ± 0.4	Soaked in deionized water beforehand. d_{in} = 2 to 3 mm.
V9	L	B	100 → 110	40 s	–1.4 to –1.6	63.3 ± 0.6	d_{in} = 2 to 3 mm, temperature not measured during charging.
V10	UH9–4	B	80 to 82	20 s	–3.1	91.3 ± 0.3	d_{in} = –150 mm. No dry runs.
V11	AV32–3	B	82	22 s	Not measured	75.9 ± 0.6	d_{in} = –150 mm. Fan cool at 8/8 speed until sample temperature reached 24 to 28 °C. Six dry runs were conducted stepping up through temperature = 60 and 70 °C.
V12	AV32–4	B	80	4 min	–4.4, SEM	68.2 ± 1.9	d_{in} = –150 mm. Fan cooled to 25 °C. Two-minute rest after cool before removal from holder. Plies repelled after previous run. Three dry runs totaling to ~200 seconds at ~80 °C.
V13	UH5–2	D	99 → 110	10 s	VSERM	83.6 ± 0.2	d_{in} = –2 mm. Moderate movement. Two dry runs at 80 °C (~400 seconds total) and one at 100 °C (~30 s) → –3.2 to –3.6 kV.
V14	SW2	D	105 → 115	30 s	Not measured	90.0 ± 0.5	d_{in} = –2 mm. Moderate movement.
V15	AV32–4	D	120	30 s	Not measured, SEM	77.9 ± 1.2	Not discharged prior to trial. d_{in} = –2 mm.

[a]Strong electrostatic movement (SEM). Very strong electrostatic repulsive movement (VSERM). Was not quantified with static meter (not measured).

Initial experiments using Ionic-Dryer Arrangement 1 attempted to achieve relatively high temperature. This was based on others' results (Ref. 26) where the highest charge density was achieved with the highest charging temperature tested, 140 °C. In the present study, attempts to maintain a 140 °C charging temperature usually resulted in small holes in the coupon due to very localized melting of the filter material from nonuniform heating. A radial thermal gradient within the hot airstream was suspected to have contributed to this problem. The melting problem was usually avoided by lowering the holding temperature to 120 °C and good filtration results were achieved from trials V1 and V2 at 89.1 and 84.9 percent FE, respectively. Moreover, each of these samples also underwent 110 min of loading testing. The results are plotted in Figure 8. It can be seen that FE values close to the instantaneous results were retained throughout. A lower proportion of particles being captured compared to the control sample might be associated with the greater stability (and smaller slope) of the V1 and V2 pressure-drop data that implied negligible clogging. However, further trials with Ionic-Dryer Arrangement 1 were not continued due to difficulty with gripping the sample during further attempts.

Although the sample gripping problem was solved with Ionic-Dryer Arrangement 2, localized melting was sometimes still an issue at 120 °C target temperature, therefore, 105 °C was targeted during trials V3 to V9. These trials investigated effects of charging time, Volare® velocity setting, not interrupting the hot-air flux during a longer charging period (trial V9), and the depth of nozzle insertion into the sample holder borehole. The latter is thought to have affected the air pressure on the coupon, thus, the aerodynamic force for embedding charges in the fibers. In trial V8, an attempt was made at using fast evaporation of water from the filter porosity with the intent being to triboelectrically assist the charging of the filter. However, this did not produce a good result. After trial V9, the ionic-dryer method was temporarily abandoned because the experimental knobs associated with the highest temperature condition practically achievable (which was perceived as being most desirable) were all tested.

Near the end of the study, trials with the ionic-dryer method resumed after relatively good results were achieved with corona-based methods at a lower ~80 °C temperature. Trials V10 to V12 targeted this temperature by backing the nozzle away to a large standoff distance from the borehole of the sample holder. Although the best Volare® result was achieved (91.3 percent FE), the associated short time (~20 s) produced inconsistent results and filtration performance was worse after a longer charging time of 4 min despite the achievement of a –4.4 kV coupon surface potential, that is, the greatest magnitude measured throughout the entire study. In trials V13 to V15, the standoff distance was drastically reduced to roughly 2 mm and higher charging temperatures were tried again. Good charging appeared to have been achieved based on surface potential measurements and coupon movement. But as before, FE values varied considerably and did not monotonically correlate with those characteristics.

3.6 Trials With Ionic Flat Iron Hair Straighteners

The flat iron hair straighteners were found to have a modest impact and boost to the charge and performance of alcohol-discharged N95 PP media, respectively. The Bio Ionic® was used to impart a positive charge at the lowest temperature setting, which is nominally 265 °F (129 °C). The potential ranged from +1.8 to +2.1 kV, and the two plies comprising the coupon repelled each other from the strong electrostatic repulsion. Three days later, FE was determined to be 63 percent. Although this amounts to a significant improvement over alcohol-discharged performance, it is also far beneath the 95 percent goal. It is supposed that the underwhelming performance is due to a lack of charging on fibers underneath the outer surfaces of the nonwoven fabric. Also, at least some of the FE increase may be due to visually undetected melting since the pressure drop was 8.9 ± 0.1 mm H_2O, which was significantly above the usual range.

Additional charging attempts with the Bio Ionic® at 265 °F (129 °C) were made but none resulted in a charge as great as that achieved for the filtration-tested sample. Further attempts were also made at the next highest temperature setting of 280 °F (138 °C). However, these were soon discontinued because lingering during swiping sometimes resulted in partial melting of filter samples, which suggested some discrepancy between actual and nominal temperature.

The BLPNTP3100 iron appeared to produce a greater flux than the Pritech iron based on probing with the static meter. Therefore, the BLPNTP3100 was chosen for charging attempts, and the Pritech was not used further. However, the best charging result achieved with the BLPNTP3100 was –0.5 kV, which corresponded to weak movement. Filtration testing of this coupon yielded 39 percent FE. These relatively poor results are attributed to the unidirectional flux of negative ions from the ion emitter being unable to uniformly charge the coupon. Also, melting was strongly suspected although visually undetected since the pressure drop was 13.7 ± 0.1 mm H_2O.

Trials were also performed on the commercial fabrics and the results are given in Table VI. Charging temperatures were based on trial and error informed by differential thermal analysis to identify temperatures just shy of the onsets of melting transitions of the different fabrics.

TABLE VI.—RESULTS OF CHARGING TRIALS ON COMMERCIALLY AVAILABLE FABRICS

[The values given after the ± symbol are one standard deviation based on two or three filtration measurements.]

Fabric	Method	Single-layer surface potential, kV		Number of layers used in filter test		Pressure drop, mm H_2O		Filtration efficiency, percent	
		As received	Charged	As received	Charged	As received	Charged	As received	Charged
97% cotton 3% spandex	Bio Ionic® 340 °F (171 °C)	+0.04	+2.0	1	1	6.89	6.46	1.6 ± 2.0	8.6 ± 1.8
95% nylon 5% spandex	Bio Ionic® 410 °F (210 °C)	–0.09 to –0.18	+1.75	1	1	7.3	8.0 ± 1.1	9.9 ± 1.2	13.0 ± 3.9
100% polyester #1721-9569	Bio Ionic® 265 °F (129 °C)	–0.25	+2.2, +3.0, +3.0	3	3	56.8 ± 0.2	69.7 ± 0.2	28.6 ± 0.8	43.9 ± 4.3
100% polyester #0074-0647	Bio Ionic® 265 °F (129 °C)	–0.5	+2, +2, +2, +2	5	4	8.15 ± 0.02	8.9 ± 0.2	19.1 ± 1.2	46.5 ± 2.1

All fabric materials exhibited significant electrostatic movement immediately after initial charging performed just prior to a weekend. Such movement was particularly pronounced for the polyesters and an example of this is shown in Video 4. On the following Monday, the movement for the cotton and nylon fabrics had significantly declined. Initial potentials of +1.3 and +2.9 kV for cotton and nylon, respectively, decayed to –0.02 and +0.7 kV 3 days later. Prior to filtration testing, these fabrics were recharged to the potentials given in Table VI. In contrast, the polyester materials mostly retained their movement and were not recharged prior to filtration testing 3 days later. Polyester layers were charged individually and then assembled into stacks for filtration testing since the stock material was extremely thin.

The filtration data suggests that the FE might have increased slightly for the cotton and nylon fabrics, but the standard deviations are too large to conclusively establish an improvement. For these fabrics, the potential slight improvement to the FE values that might be provable with more testing does not seem to justify the effort of charging. On the other hand, both polyesters exhibited significant improvements in FE after charging. However, while the pressure drop is reasonably low for the stack of polyester #0074-0647 layers, it is rather high and perhaps untenable for the stack of polyester #1721-9569 layers. Therefore, only the polyester #0074-0647 appears to have potential utility as a charged material for facemasks. Although the corresponding FE of 46.5 percent is well beneath that of an N95 mask, this offers a significant performance boost at a similar pressure drop compared to cotton. However, the robustness of the boosted performance relative to loading and possible discharge from breathed vapors or contact with or proximity to the human body and metal objects was not investigated.

4.0 Concluding Remarks and Future Work

Polypropylene (PP) media from N95 masks were recharged to an extent that significantly improved filtration performance versus the discharged state. Setups using corona discharge or an ionic hair dryer in various electrode configurations and parameter combinations gave better results than the ionic hair straighteners. However, recharging to a degree that is sufficient to meet the N95 requirement of filtration efficiency (FE) ≥ 95 percent is a nontrivial challenge not overcome in this study. Therefore, improvements to these recharging processes would be needed for broad scalability. Here, all coupons were hot while charging to a single charge polarity. Future investigators should consider bipolar charging without heating.

In this study, all of the charging processes employed resulted in demonstrable electrostatic movement and large changes to the surface potentials of recharged coupons. While recharged coupons also exhibited significant improvement of FE versus discharged coupons, the values of surface potentials did not straightforwardly correlate to filtration performance. For example, several trials (e.g., V12, C9, C26, and C32) resulted in FEs that were much lower than what might be expected from the apparently high coupon surface potential after charging. The lack of direct correlation is attributed to (1) nonuniform charging of the media, (2) charge decay to the environment during the time lag before filtration measurement, and (3) the imperfect accuracy and partial bleeding of charge by the handheld potential meter. However, it can be said that recharged PP coupons exhibiting FE ≥ 80 percent tended to, but did not always, have surface potential magnitude ≥2 kV.

For corona discharges using one of the custom point-source configurations designed and built in the lab, 80 percent of charging trials yielded FE ≥ 80 percent. A wide variety of parametric and configuration variants were employed throughout these trials and no conclusions were drawn about the optimal condition. A large number of variables were at play (perhaps some lurking), and significant changes to the method often resulted in very similar FE results. However, there were a significant number of trials exhibiting such moderate success performed at 80 °C. Therefore, 80 °C appears to be a viable charging temperature for a FE ≥ 80 percent standard of performance and a possible starting point for future work pursuing hot charging. Also, similar future experiments that target full-size N95 masks might benefit from contorting the masks into a roughly hemispherical shape during charging as long as the masks could be durably reshaped for good facial fit afterwards. Both reshaping processes might be performed with three-dimensional- (3D-) printed fixtures. The purpose of the hemispherical shape would be to provide for an electric field having relatively good uniformity via a well-placed sharp emitter tip and a hemispherical counter electrode, for example, made of metal screen.

Charging trials performed with the ionic hair dryer resulted in just under half of the coupons having FE ≥ 80 percent and more variation in the resulting performance of recharged coupons, which spanned 60 to 91 percent FE. This is attributed to variation in and lack of precise control over the coupon temperature and aerodynamic force by which charges were imparted to PP coupons during the charging process. That three trials (V1, V10, and V14) achieved FE ≥ 90 percent (within statistical variation) demonstrates that relatively good results are possible with this method, and any future pursuits should consider work to improve control over the process. One approach, which could also be adapted to a full-size N95 mask, involves 3D printing a new fixture for controllably and uniformly passing hot ionized air through the filter while filter temperature is monitored via infrared thermometer. Such a fixture might combine design elements of (1) Figure 7 to hold the mask or coupon and (2) the funnels shown in (see Figure 2(b), (c), and (d)) to guide the airflow.

The hair straighteners that used a triboelectric-rubbing mechanism capably imparted positive charge to media. Straighteners employing an ion emitter were not effective because they could not provide uniform exposure to coupons. Of all the charging methods tried, such triboelectric rubbing provided the least improvement to the FE of discharged PP coupons. This is probably because the process only accessed the fibers on the opposing outer surfaces of the nonwoven mat and missed fibers buried within the mat thickness. However, such triboelectric rubbing did provide a significant FE performance improvement to polyester fabric #0074-0647. This process could be performed by a layperson for the construction of a homemade mask with a reasonably low pressure drop and significantly better FE compared to one made of cloth. However, the use of high-quality masks such as N95s is much preferred over this option due to their superior performance.

Appendix—Videos

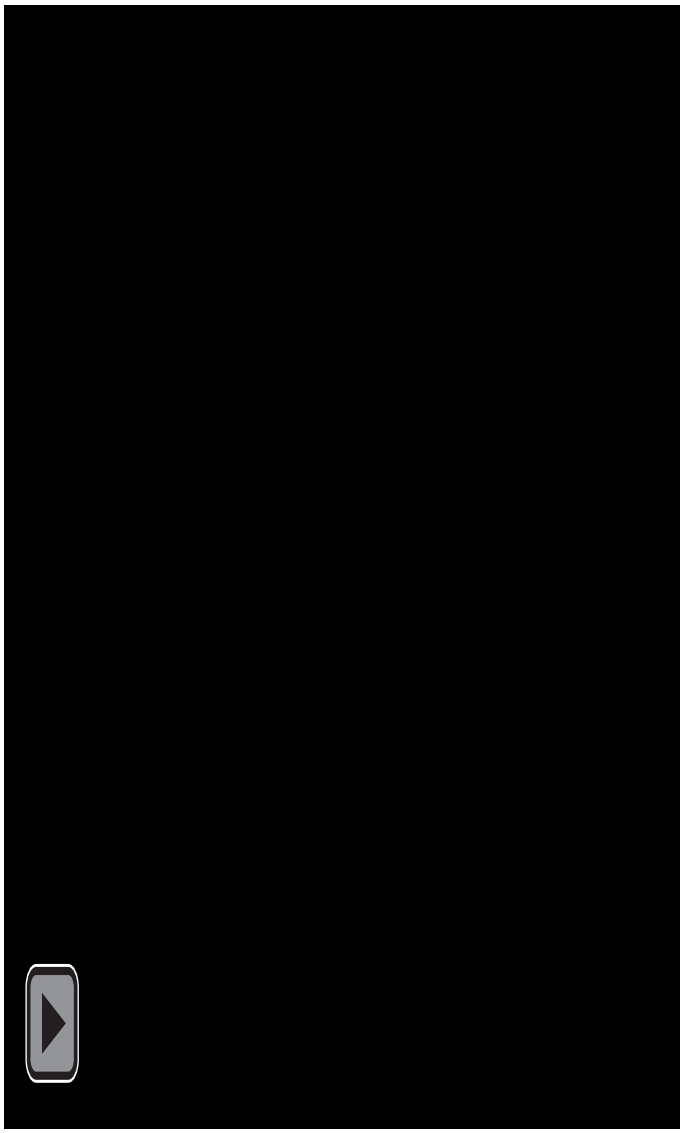

Video 1.—Moderate electrostatic movement for recharged polypropylene a few days after being recharged.

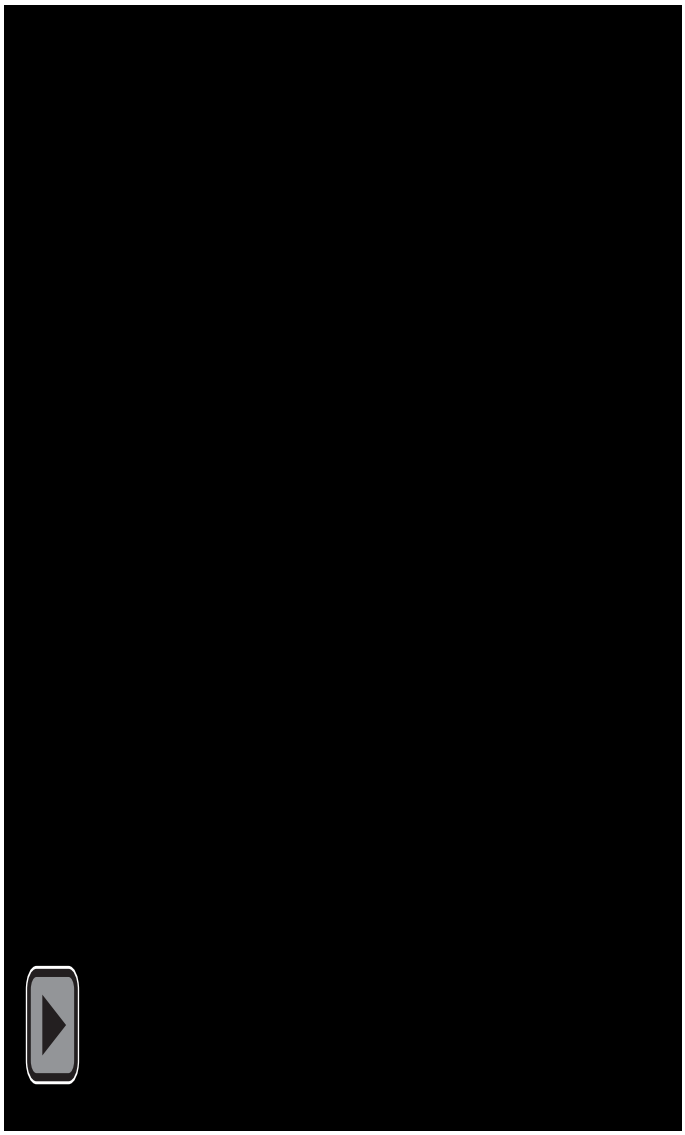

Video 2.—Static meter showing strong flux of negative ions in airflow of BaBylissPRO® Volare® V1 ionic dryer.

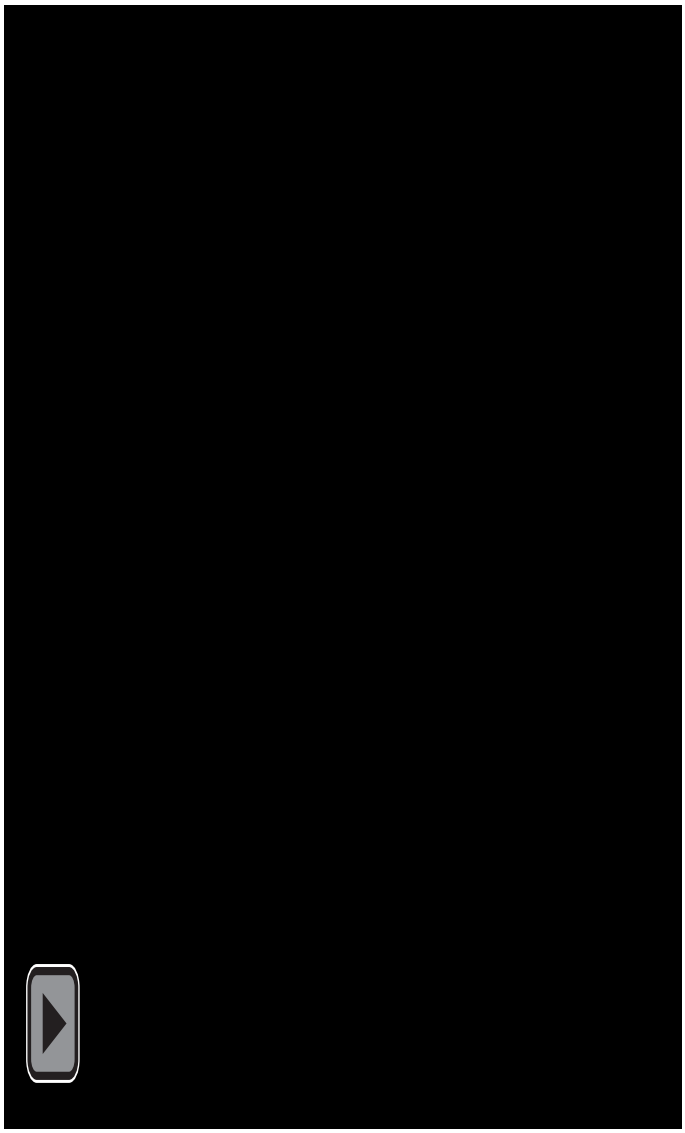

Video 3.—Static meter showing flux of negative ions for Nano Titanium™ Prima3100™ 1-in. (25.4-mm) model (BLPNTP3100).

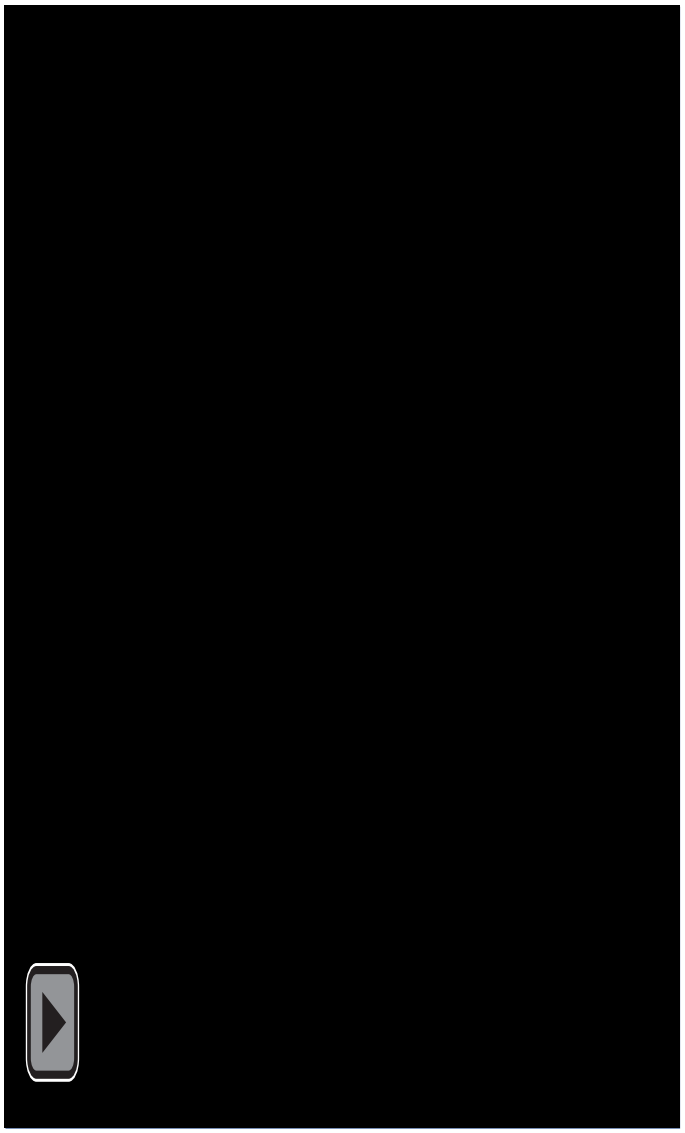

Video 4.—Electrostatic movement in a single layer of polyester fabric (#0074-0647).

References

1. National Institute for Occupational Safety and Health: Determination of Particulate Filter Efficiency Level for N95 Series Filters Against Solid Particulates for Non-Powered, Air-Purifying Respirators Standard Testing Procedure (STP). TEB–APR–STP–0059, Rev. 3.2, 2019.
2. Rengasamy, Samy, et al.: A Comparison of Facemask and Respirator Filtration Test Methods. J. Occup. Environ. Hyg., vol. 14, no. 2, 2017, pp. 92–103. https://doi.org/10.1080/15459624.2016.1225157
3. Viscusi, Dennis J.; King, William P.; and Shaffer, Ronald E.: Effect of Decontamination on the Filtration Efficiency of Two Filtering Facepiece Respirator Models. J. Int. Soc. Respir. Prot., vol. 24, no. 15, 2007, pp. 93–107.
4. Liao, Lei, et al.: Can N95 Respirators Be Reused After Disinfection? And for How Many Times? Occupational and Environmental Health, preprint, 2020. https://doi.org/10.1101/2020.04.01.20050443
5. Ghosal, Arkaprovo, et al.: Numerical Prediction of the Effect of Uptake Velocity on Three-Dimensional Structure, Porosity and Permeability of Meltblown Nonwoven Laydown. Polymers, vol. 85, 2016, pp. 19–27. https://doi.org/10.1016/j.polymer.2016.01.013
6. Brown, R.C.: The Behaviour of Fibrous Filter Media in Dust Respirators. Ann. Occup. Hyg., vol. 23, no. 4, 1980, pp. 367–380.
7. Zangmeister, Christopher D., et al.: Filtration Efficiencies of Nanoscale Aerosol by Cloth Mask Materials Used to Slow the Spread of SARS-CoV-2. ACS Nano, vol. 14, no. 7, 2020, pp. 9188–9200. https://doi.org/10.1021/acsnano.0c05025
8. Lee, Jinwook; and Kim, Jooyoun: Material Properties Influencing the Charge Decay of Electret Filters and Their Impact on Filtration Performance. Polymers, vol. 12, no. 721, 2020. https://doi.org/10.3390/polym12030721
9. Wang, Chiu-Sen: Electrostatic Forces in Fibrous Filters—A Review. Powder Technol., vol. 118, nos. 1–2, 2001, pp. 166–170. https://doi.org/10.1016/S0032-5910(01)00307-2
10. Hoppel, William A.; and Frick, Glendon M.: Ion—Aerosol Attachment Coefficients and the Steady-State Charge Distribution on Aerosols in a Bipolar Ion Environment. Aerosol Sci. Tech., vol. 5, no. 1, 1986, pp. 1–21. https://doi.org/10.1080/02786828608959073
11. Fuchs, N.A.: On the Stationary Charge Distribution on Aerosol Particles in a Bipolar Ionic Atmosphere. Geofis. Pura Appl., vol. 56, no. 1, 1963, pp. 185–193. https://doi.org/10.1007/BF01993343
12. Jasper, Warren J., et al.: Degradation Processes in Corona-Charged Electret Filter-Media With Exposure to Ethyl Benzene. J. Eng. Fibers Fabr., vol. 2, no. 4, 2007. https://doi.org/10.1177/155892500700200401
13. Baumgartner, H.-P.; and Loffler, F.: The Collection Performance of Electret Filters in the Particle Size Range 10 nm–10 μm. J. Aerosol Sci., vol. 17, no. 3, 1986, pp. 438–445.
14. Tsai, Peter P.; Schreuder-Gibson, Heidi; and Gibson, Phillip: Different Electrostatic Methods for Making Electret Filters. J. Electrostat., vol. 54, nos. 3–4, 2002, pp. 333–341. https://doi.org/10.1016/S0304-3886(01)00160-7
15. Jasper, W.: Electret Science, Engineering, and Manufacturing of N95 Masks. Private communication, 2020.
16. Gross, B.; and Denard, L. Ferreira: On Permanent Charges in Solid Dielectrics I. Dielectric Absorption and Temperature Effects in Carnauba Wax. Phys. Rev., vol. 67, nos. 7–8, 1945, pp. 253–259. https://doi.org/10.1103/PhysRev.67.253
17. Eguchi, Mototaro: On the Permanent Electret. Philos. Mag., vol. 49, 1925, pp. 178–192.
18. Partington, J.R.; Planer, G.V.; and Boswell, I.I.: Surface Charge of 'Electrets.' Nature, vol. 158, 1946, pp. 835–836. https://www.nature.com/articles/158835b0 Accessed Jan. 10, 2022.
19. Gross, B.: On Permanent Charges in Solid Dielectrics. II. Surface Charges and Transient Currents in Carnauba Wax. J. Chem. Phys., vol. 17, no. 10, 1949, pp. 866–872. https://doi.org/10.1063/1.1747079
20. Tsai, Peter Ping-yi; Qin, Guo-wei; and Hassenboehler, Charles: Comparison of Electrostatic Charging at Different Locations in the Melt Blowing Process. International Nonwovens Journal, vol. os-9, no. 3, 2000. https://doi.org/10.1177/1558925000OS-900304
21. Tsai, P.; Qin, G.; and Wadsworth, L.: Theory and Techniques of Electrostatic Charging of Melt-Blown Nonwoven Webs. Tappi J., vol. 81, 1998, pp. 274–278.
22. Dascalescu, L., et al.: Corona Charging of Composite Non-Woven Media for Air Filtration. Proceedings ESA Annual Meeting on Electrostatics, no. D3, 2010.
23. Giacometti, Jose A.; and Campos, J. Sinézio Carvalho: Constant Current Corona Triode With Grid Voltage Control. Application to Polymer Foil Charging. Rev. Sci. Instrum., vol. 61, no. 3, 1990, pp. 1143–1150. https://doi.org/10.1063/1.1141438
24. Tsai, Peter P.; and Wadsworth, Larry C.: Method and Apparatus for the Electrostatic Charging of a Web or Film. U.S. Patent 5,401,446, March 1995.
25. Mellinger, Axel: Charge Storage in Electret Polymers: Mechanisms, Characterization and Applications. Dr. Rer. Nat. Habil., Universitat Potsdam, 2004.
26. Kravtsov, A., et al.: The Electret Effect in Polypropylene Fibers Treated in a Corona Discharge. Adv. Polym. Technol., vol. 19, no. 4, 2000, pp. 312–316.

27. Zhang, Haifeng, et al.: Design of Electret Polypropylene Melt Blown Air Filtration Material Containing Nucleating Agent for Effective PM2.5 Capture. RSC Adv., vol. 8, no. 15, 2018, pp. 7932–7941. https://doi.org/10.1039/C7RA10916D
28. Gerhard-Multhaupt, R., et al.: High Space-Charge Densities in the Bulk of Fluoropolymer Electrets Detected With Piezoelectrically Generated Pressure Steps. Space Charge in Solid Dielectrics, J.C. Fothergill and L.A. Dissado, eds., Dielectrics Society, 1998, pp. 123–132.
29. von Seggern, Heinz: Isothermal and Thermally Stimulated Current Studies of Positively Corona Charged Polyfluoro–ethylenepropylene (Teflon FEP). J. Appl. Phys., vol. 52, no. 6, 1981, pp. 4081–4085. https://doi.org/10.1063/1.329257
30. Remke, R.L.; and von Seggern, H.: Modeling of Thermally Stimulated Currents in Polytetrafluoroethylene. J. Appl. Phys., vol. 54, no. 9, 1983, pp. 5262–5266. https://doi.org/10.1063/1.332702
31. Nath, R.; and Perlman, M.M.: Effect of Crystallinity on Charge Storage in Polypropylene and Polyethylene. IEEE Trans. Elect. Insul., vol. 24, no. 3, 1989, pp. 409–412. https://doi.org/10.1109/14.30881
32. Gonzalez, Francisco Camacho: Charge-Storage Mechanisms in Polymer Electrets. Doctor of Natural Sciences thesis, 2006.
33. Fillard, J.P.; and van Turnhout, J.: Thermally Stimulated Processes in Solids: New Prospects. Proceedings of the International Workshop on Thermally Stimulated Processes in Solids, Elsevier Scientific Publishing Company, Amsterdam, 1977.
34. Kao, K.C.; and Hwang, W.: Electrical Transport in Solids, With Particular Reference to Organic Semiconductors. Pergamon Press, New York, NY, 1981.
35. Motyl, Edmund; and Lowkis, Bozena: Effect of Air Humidity on Charge Decay and Lifetime of PP Electret Nonwovens. Fibres Text. East. Eur., vol. 14, no. 5, 2006, pp. 39–42.
36. Tennal, K., et al.: Effect of Loading With an Oil Aerosol on the Collection Efficiency of an Electret Filter. Particul. Sci. Technol., vol. 9, 1991, pp. 19–29.
37. Mahdavi, Alireza, et al.: Particle Loading Time and Humidity Effects on the Efficiency of an N95 Filtering Facepiece Respirator Model Under Constant and Inhalation Cyclic Flows. Ann. Occup. Hyg., vol. 59, no. 5, 2015, pp. 629–640. https://doi.org/10.1093/annhyg/mev005
38. Centers for Disease Control and Prevention: NIOSH Guide to the Selection and Use of Particulate Respirators. Certified Under 42 CFR 84, DHHS Publication 96–101, 1996. https://www.cdc.gov/niosh/docs/96-101/default.html
39. Worton, David R., et al.: Lubricating Oil Dominates Primary Organic Aerosol Emissions From Motor Vehicles. Environ. Sci. Technol., vol. 48, no. 7, 2014, pp. 3698–3706. https://doi.org/10.1021/es405375j
40. Blackford, D.B., et al.: Alteration in the Performance of Eletrostatic Filters Caused by the Exposure to Aerosols. Paper presented at the 4th World Filtration Congress, Royal Flemish Society, Belgium, 1986.
41. Gao, Shuang, et al.: Performance of N95 FFRs Against Combustion and NaCl Aerosols in Dry and Moderately Humid Air: Manikin-Based Study. Ann. Occup. Hyg., vol. 60, no. 6, pp. 748–760. https://doi.org/10.1093/annhyg/mew019
42. He, Xinjian: Laboratory Evaluation of the Particle Size Effect on the Performance of an Elastomeric Half-Mask Respirator Against Ultrafine Combustion Particles. Ann. Occup. Hyg., vol. 57, no. 7, 2013, pp. 884–897. https://doi.org/10.1093/annhyg/met014
43. Lee, Bruce Y.: Wildfire Smoke: Here Is Another Reason More N95 Face Masks Are Needed. Forbes, 2020. https://www.forbes.com/sites/brucelee/2020/09/20/wildfire-smoke-here-is-another-reason-more-n95-face-masks-are-needed/?sh=56afc6db4497 Accessed April 18, 2022.
44. Barrett, Leonard W.; and Rousseau, A.D.: Aerosol Loading Performance of Electret Filter Media. Am. Ind. Hyg. Assoc. J., vol. 59, no. 8, 1998, pp. 532–539. https://www.tandfonline.com/doi/abs/10.1080/15428119891010703
45. Bergman, Michael S., et al.: Impact of Multiple Consecutive Donnings on Filtering Facepiece Respirator Fit. Am. J. Infect. Control, vol. 40, no. 4, 2012, pp. 375–380.
46. He, Xinjian, et al.: Manikin-Based Performance Evaluation of Elastomeric Respirators Against Combustion Particles. J. Occup. Environ. Hyg., vol. 10, no. 4, 2013, pp. 203–212. https://doi.org/10.1080/15459624.2012.760063
47. Rebmann, Terri; Carrico, Ruth; and Wang, Jing: Physiologic and Other Effects and Compliance With Long-Term Respirator Use Among Medical Intensive Care Unit Nurses. Am. J. Infect. Control, vol. 41, no. 12, 2013, pp. 1218–1223. https://doi.org/10.1016/j.ajic.2013.02.017
48. Wilson, Mark: Its Hard to Breathe in an N95 Mask. This Standard Scientist Has a Clever Solution. Fast Company, 2020. https://www.fastcompany.com/90509409/its-hard-to-breathe-in-an-n95-mask-this-stanford-scientist-has-a-clever-solution Accessed Nov. 23, 2021.
49. Rosner, Elisheva: Adverse Effects of Prolonged Mask Use Among Healthcare Professionals During COVID–19. J. Infect. Dis. Epidemiol., vol. 6, no. 130, 2020. https://doi.org/10.23937/2474-3658/1510130
50. Centers for Disease Control and Prevention: Implementing Filtering Facepiece Respirator (FFR) Reuse, Including Reuse After Decontamination, When There Are Known Shortages of N95 Respirators. 2020. https://www.cdc.gov/coronavirus/

2019-ncov/hcp/ppe-strategy/decontamination-reuse-respirators.html Accessed Nov. 23, 2021.
51. Allen, Jonathan; McCausland, Phil; and Farivar, Cyrus: Trump Administration Paying Huge Premium for Mask-Cleaning Machines. Which Don't Do the Job. NBC News, 2020. https://www.nbcnews.com/politics/white-house/trump-administration-paying-huge-premium-mask-cleaning-machines-which-don-n1210896 Accessed April 18, 2022.
52. Centers for Disease Control and Prevention: National Personal Protective Technology Laboratory Evaluation of Decontaminated N95 Respirators: Models 3M 1860, 3M 1870+, Halyard 46727. 2020. https://www.cdc.gov/niosh/npptl/respirators/testing/results/Decon_021_Redacted-508.pdf Accessed Jan. 12, 2022.
53. Wittry, Jan: NASA, University Hospitals Join Forces in Response to COVID–19. 2020. https://www.nasa.gov/press-release/glenn/2020/nasa-university-hospitals-join-forces-in-response-to-covid-19/ Accessed Sept. 25, 2020.
54. Oh, Chamteut, et al.: Dry Heat as a Decontamination Method for N95 Respirator Reuse. Environ. Sci. Technol. Lett., vol. 7, no. 9, 2020, pp. 677–682. https://doi.org/10.1021/acs.estlett.0c00534
55. Centers for Disease Control and Prevention: National Personal Protective Technology Laboratory Evaluation of Decontaminated N95 Respirators: Model 3M Vflex 1804. 2021. https://www.cdc.gov/niosh/npptl/respirators/testing/results/Decon_039_Redacted-508.pdf Accessed Jan. 12, 2022.
56. Juang, Pascal S.C.; and Tsai, Peter: N95 Respirator Cleaning and Reuse Methods Proposed by the Inventor of the N95 Mask Material. J. Emerg. Med., vol. 58, no. 5, 2020, pp. 817–820. https://doi.org/10.1016/j.jemermed.2020.04.036
57. Bergman, Michael S., et al.: Evaluation of Multiple (3-Cycle) Decontamination Processing for Filtering Facepiece Respirators. J. Eng. Fibers Fabr., vol. 5, no. 4, 2010. https://doi.org/10.1177/155892501000500405
58. Centers for Disease Control and Prevention: Decontamination and Reuse of Filtering Facepiece Respirators. Coronavirus Disease 2019, 2020. https://stacks.cdc.gov/view/cdc/90574 Accessed Jan. 6, 2022.
59. Centers for Disease Control and Prevention: National Personal Protective Technology Laboratory Decontaminated Assessment Results. 2021. https://www.cdc.gov/niosh/npptl/respirators/testing/DeconResults.html Accessed Jan. 12, 2022.
60. Trefethen, Lloyd: Surface Tension in Fluid Mechanics. National Committee for Fluid Mechanics Films Film Notes, No. 21610, Encyclopaedia Brittannica Educational Corporation, Chicago, IL, 1969, pp. 1–8. http://web.mit.edu/hml/ncfmf/04STFM.pdf Accessed Nov. 23, 2021.
61. Vazquez, Gonzalo; Alvarez, Estrella; and Navaza, Jose M.: Surface Tension of Alcohol Water + Water From 20 to 50 Degree C. J. Chem. Eng. Data, vol. 40, no. 3, 1995, pp. 611–614. https://doi.org/10.1021/je00019a016
62. Hossain, Emroj, et al.: Recharging and Rejuvenation of Decontaminated N95 Masks. Phys. Fluids, vol. 32, no. 093304, 2020. https://doi.org/10.1063/5.0023940
63. Choi, Hyun-Jin, et al.: Experimental Study on Charge Decay of Electret Filter Due to Organic Solvent Exposure. Aerosol Sci. Tech., vol. 49, no. 10, 2015, pp. 977–983. https://doi.org/10.1080/02786826.2015.1086724
64. Santos, Leandra P., et al.: Water With Excess Electric Charge. J. Phys. Chem. C, vol. 115, no. 22, 2011, pp. 11226–11232. https://doi.org/10.1021/jp202652q
65. Jasper, W., et al.: Effect of Xylene Exposure on the Performance of Electret Filter Media. J. Aerosol Sci., vol. 37, no. 7, 2006, pp. 903–911. https://doi.org/10.1016/j.jaerosci.2005.06.008
66. National Oceanic and Atmospheric Administration: Dioctyl Phthalate datasheet, 1999. https://cameochemicals.noaa.gov/chris/DOP.pdf Accessed Nov. 23, 2021.
67. Topas GmbH: Di-Ethyl-Hexyl-Sebacate datasheet, 2019. https://www.topas-gmbh.de/wordpress/dateien/produkte/DEHS_Datasheet_eng.pdf Accessed Nov. 23, 2021.
68. Sugihara, K.: Recharging N95 Masks Using a Van de Graaff Generator for Safe Recycling. Soft Matter, no. 1, 2021. https://doi.org/10.1039/D0SM02004D
69. Herb, R.G.: Van de Graaff Generators. Nuclear Instrumentation I/Instrumentelle Hilfsmittel der Kernphysik I, E. Creutz, ed., Vol. 8, Springer, Berlin, Heidelberg, 1959, pp. 64–104. https://link.springer.com/book/10.1007%2F978-3-642-45926-9 Accessed Nov. 23, 2021.
70. Schumaker, Erin: DIY Masks May Not Protect You From COVID–19. But Here's Why It's Smart To Wear One. ABC News, 2020. https://abcnews.go.com/Health/diy-masks-protect-covid-19-smart-wear/story?id=69957443 Accessed Nov. 23, 2021.
71. Godoy, Maria: With Omicron, You Need a Mask That Means Business. NPR, Washington, DC, 2021. https://www.npr.org/sections/health-shots/2021/12/23/1066871176/mask-n95-omicron-contagious Accessed Jan. 12, 2022.
72. Stewart, Emily: Anti-Maskers Explain Themselves. Vox, 2020. https://www.vox.com/the-goods/2020/8/7/21357400/anti-mask-protest-rallies-donald-trump-covid-19 Accessed Nov. 23, 2020.
73. Konda, Abhiteja, et al.: Response to Letters to the Editor on Aerosol Filtration Efficiency of Common Fabrics Used in Respiratory Cloth Masks: Revised and Expanded Results.

ACS Nano, vol. 14, no. 9, 2020, pp. 10764–10770. https://doi.org/10.1021/acsnano.0c04897
74. Electron Work Function of the Elements. Washington State University. https://public.wsu.edu/~pchemlab/documents/Work-functionvalues.pdf Accessed Sept. 28, 2020.
75. Chrzanowski, J.; Kravtsov, Y.; and Bieg, B.: Application of the Work Function to Study the Percentage Composition of Aluminum Alloys. Zeszyty Naukowe/Maritime University of Szczecin, vol. 38, no. 110, 2014, pp. 27–31. http://yadda.icm.edu.pl/yadda/element/bwmeta1.element.baztech-64a52c00-e89a-4da6-967b-409a8705c643 Accessed Nov. 23, 2021.
76. Alchagirov, B.B., et al.: Electron Work Function in Alloys From the Tin-Lead System. Tech. Phys., vol. 51, 2006, pp. 1624–1626. https://doi.org/10.1134/S1063784206120127 Accessed Nov. 23, 2021.
77. National Institute for Occupational Safety and Health: Determination of Particulate Filter Efficiency Level for N95 Series Filters Against Solid Particulates for Non-Powered, Air-Purifying Respirators Standard Testing Procedure (STP). Procedure No. TEB–APR–STP–0059, 2019. https://www.cdc.gov/niosh/npptl/stps/pdfs/TEB-APR-STP-0059-508.pdf Accessed Nov. 23, 2021.
78. Li, Lin, et al.: Evaluation of Filter Media for Particle Number, Surface Area and Mass Penetrations. Ann. Occup. Hyg., vol. 56, no. 5, 2012, pp. 581–594. https://doi.org/10.1093/annhyg/mes034
79. Eninger, Robert M., et al.: What Does Respirator Certification Tell Us About Filtration of Ultrafine Particles? J. Occup. Environ. Hyg., vol. 5, no. 5, 2008, pp. 286–295. https://doi.org/10.1080/15459620801960153
80. Xu, Dexuan, et al.: Discharge Characteristics of Magnet Enhancement Corona Discharges. Recent Developments in Applied Electrostatics, Proceedings of the Fifth International Conference on Applied Electrostatics, Shanghai, China, 2004, pp. 65–68. https://www.sciencedirect.com/science/article/pii/B9780080445847500165 Accessed Nov. 24, 2021.